



Multi-physics coupling simulation of GMAW arc and droplet behaviors based on CFD

Zhang Yujiao¹ · Li Yinghao¹ · Niu Sizhe¹ · Wang Hongtao¹ · Zong Ran¹

Received: 23 October 2023 / Accepted: 26 June 2024 / Published online: 17 July 2024
© International Institute of Welding 2024

Abstract

A three-dimensional transient model of gas metal arc welding (GMAW) process including the arc plasma and droplet transfer was established to investigate the complex coupling mechanism of mass transfer, heat transfer, electromagnetism, and hydrodynamics. The arc shape, current density, temperature field, electromagnetic force, arc pressure and droplet behavior were analyzed. The results showed that the iron vapor generated on the droplet surface and diffused in the arc, which changed the plasma thermal-pressure distribution. The upward surface tension maintained the forming droplet at the wire tip. The electromagnetic force promoted necking, resulting in a decrease in surface tension. Gravity and plasma drag force accelerated the droplet. The behaviors of the inner arc layer varied periodically with the droplet transfer, while the arc periphery remained stable. Droplet transfer was the result of periodic changes in the resultant of all external forces over time, which also led to periodic changes in arc behavior. This study laid the foundation for further research on the influence of arc and droplet behaviors on the weld pool.

Keywords GMAW · droplet transfer · numerical simulation

1 Introduction

GMAW referred to a method that used the arc between the wire and the workpiece as a heat source to melt the metal [1, 2]. It was widely used in industrial manufacturing due to the advantages of good welding quality, high efficiency, and easy automation [3]. The stability and quality of arc welding process were related to arc and droplet transfer behavior. A thorough understanding of arc and droplet transition behavior is the basis of optimizing GMAW process. It was

difficult to analyze it accurately only through experimental observation. Using numerical simulation to investigate the behaviors of GMAW arc and droplet and reveal their physical properties had become a hot topic [4].

Murphy [5] et al. established a three-dimensional computational model of gas-metal arc, that included wire electrode, arc plasma and weld pool. The results showed that the temperature and current density distribution of the weld pool were closely related to the arc behavior. The flow direction in the weld pool was affected by the droplet impact. Zhao [6] et al. established a unified numerical model including the interaction between the arc plasma and the moving droplet to research welding phenomenon under the variable polarity GMAW (VP-GMAW). The arc and droplet transfer behavior varied under different current polarities. Applying negative electrode polarity could shrink the arc shape, reduce the temperature and speed of the arc plasma. Under the same average welding current, the droplet size obtained by VP-GMAW was larger and the temperature is lower than that of DC-GMAW. L, Wang et al. used fluent software to study the influence of applied magnetic field on the droplet transition, and pointed out that the change of arc plasma force is the reason for the change of the droplet transfer frequency size and tilt Angle [7].

Recommended for publication by Commission II - Arc Welding and Filler Metals

Highlights

- The generation, distribution and influence of iron vapor are analyzed in detail.
- The periodicity of arc and droplet behavior is analyzed and clarified.

✉ Zong Ran
zongran@sdut.edu.cn

¹ School of Mechanical Engineering, Shandong University of Technology, Zibo 255000, People's Republic of China

Droplet transfer was one of the key factors affecting the stability of GMAW and the quality of weld joints. The theories of droplet transfer included static force balance theory (SFBT) [8], pinch instability theory (PIT) [9], “mass-spring” theory [10], energy minimum theory and fluid dynamics theory. The fluid dynamics theory combined the continuity equation and momentum conservation equation to analyze the growth and transition process of the droplet, which could effectively calculate the flow inside the droplet and the dynamic behavior of the droplet transfer. Volume of fluid (VOF) [11] introduced a volume fraction F to calculate the surface profile, which the most widely used method in the theory of fluid dynamics. Choi [12] and Fan [13] et al. used the VOF theory to calculate the droplet transfer frequency and its internal thermal behavior, and the simulation results were in good agreement with the experimental results.

During GMAW process, the high temperature molten metal vaporized into metal vapor and diffused in the arc, which differed greatly from the physical characteristics of shielding gas in terms of ionization energy, excitation energy, etc. The metal vapor in the arc changed the physical parameters of the plasma, the conductivity of the arc center decreased, and the current density distribution shrank [14]. The metal vapor in the arc core increased the thermal radiation in the arc core, which affected the arc temperature distribution [15]. The presence of metal vapor also caused the current path to expand upwards, increasing the electromagnetic force on the droplet and shortening the droplet transfer period [16]. Nomura [17] et al. measured that the iron vapor mass fraction (Y_m) in the arc changed with the waveform of pulse current. It was necessary to calculate the iron vapor generated on the surface of droplet and weld pool. L, L, Wang [18] et al. found that the iron vapor generated by the droplet was more than that of the weld pool. It was difficult to measure the iron vapor distribution in the arc because of the high-speed movement of the droplet [19]. Schnick [20, 21] et al. simulated the influence of iron vapor on the arc and found that the iron vapor continuously generated by the droplet, which could shrink the arc and reduce its thermal efficiency. Haidar [22] et al. calculated the iron vapor distribution based on the droplet surface temperature and found that it could reduce the velocity of plasma. Hertel [23] et al. simulated the droplet transfer in the GAMW-P and pointed out that the vaporization of the droplet absorbed heat and suppressed the droplet spattering. Ogino [24] et al. calculated the iron vapor generated during the droplet transfer step-by-step and found that the increase of Y_m reduced the plasma electrical conductivity and enhanced the electromagnetic force at the neck, thereby promoting the droplet transfer. The above research showed that the iron vapor had an important impact on the arc and droplet behaviors.

However, it was difficult to observe the distribution of iron vapor through experiments, and step-by-step modeling based on different droplet states required a large amount of calculation and complicated modeling work.

A three-dimensional transient “arc-droplet” multi-physics coupling model was established. The distribution of iron vapor in the arc was calculated by User-Defined Scalar (UDS) transport equations. The influence of iron vapor on electric conductivity and radiation coefficient of arc plasma was considered. The arc thermal-pressure distribution and droplet transfer were quantitatively analyzed. The simulation results were in good agreement with the measurement by high-speed camera.

2 Mathematical modelling

2.1 Assumption

The GAMW arc and droplet behaviors involved complex mass and heat transfer processes that were difficult to fully consider in a mathematical model. To simplify the calculation, the following assumptions were followed [25]:

- (1) Arc and droplet were axisymmetric.
- (2) The fluid in the calculation area was laminar and continuous. The surface tension coefficient was constant. The other thermodynamic properties of metal and plasma were simplified as a function of temperature and Y_m [19, 26]. The nomenclatures and constants used in the model were listed in Table 1.
- (3) The plasma was in a local thermal equilibrium state, the various particles from the Y_m are treated as homogenous particles and are electrically neutral.
- (4) The workpiece was kept flat, ignoring the influence of the weld pool surface deformation on the arc. Mass loss due to phase transition of droplet was ignored.

2.2 Governing equations

Based on the above assumptions, the governing equations of the GMAW were established in the Cartesian coordinate system.

- (1) Continuity equation (Eq. 1)

$$\frac{\partial \rho}{\partial t} + \nabla \cdot (\rho v) = S_m \quad (1)$$

where S_m was the mass source of droplet. It was calculated by Eq. 2.

$$\iiint S_m = \pi \rho r_w^2 v_w \quad (2)$$

- (2) Momentum conservation equation (Eq. 3)

Table 1 Nomenclatures and constants used in the simulation model

Symbol	Nomenclature	Symbol	Nomenclature
A	Magnetic vector potential (Wb·m ⁻¹)	<i>S_m</i>	Mass source (kg·m ⁻³ ·s ⁻¹)
B	Magnetic flux density (T)	<i>S_{Rg}</i>	Gas radiation loss (J·m ⁻³ ·s ⁻¹)
<i>C_{ds}</i>	Resistance coefficient of the sphere	<i>S_{Rl}</i>	Liquid radiation loss (J·m ⁻³ ·s ⁻¹)
<i>C_p</i>	Specific heat (J·kg ⁻¹ ·K ⁻¹)	<i>t</i>	Time (s)
<i>D</i>	Diffusion coefficient (kg·m ⁻² ·s ⁻¹)	<i>T</i>	Temperature (K)
<i>e</i>	Electron charge (1.6 × 10 ⁻¹⁹ C)	<i>T₀</i>	Environment temperature (300K)
<i>F</i>	Volume fraction of metal phase	<i>T_l</i>	Molten metal temperature
<i>F_{em}</i>	Electromagnetic force (N·m ⁻³)	<i>T_b</i>	Boiling point of iron (3050K)
<i>F_{emx}, F_{emy}, F_{emz}</i>	Electromagnetic force at different direction (N·m ⁻³)	<i>T_w</i>	Temperature of wire (K)
<i>F_g</i>	Gravity (N)	v	Velocity vector (m·s ⁻¹)
<i>F_m</i>	Volume fraction of the metal phase	<i>v_{droplet}</i>	Droplet velocity (m·s ⁻¹)
<i>F_{pla}</i>	Plasma drag force (N)	<i>v_g</i>	Velocity of plasma (m·s ⁻¹)
<i>F_s</i>	Resultant of surface tension (N)	<i>v_{gas}</i>	Velocity of shielding gas (m·s ⁻¹)
<i>F_{ST}</i>	Surface tension force (N·m ⁻³)	<i>v_w</i>	Wire feeding rate (0.12 m·s ⁻¹)
<i>g</i>	Gravitational acceleration (9.81 m·s ⁻²)	<i>W</i>	Joule heat generation (J·m ⁻³ ·s ⁻¹)
<i>h</i>	Enthalpy (J·kg ⁻¹)	<i>x, y, z</i>	Coordinates (m)
<i>H_{vap}</i>	Latent heat of vaporization (J·kg ⁻¹)	<i>Y</i>	Mass fraction of iron vapor
<i>I</i>	Welding current (250 A)	<i>α</i>	Constant (3.11 × 10 ⁻⁴ m·A ⁻¹) [25]
j	Arc current density (A·m ⁻²)	<i>β</i>	Constant (4.63 × 10 ⁻⁵ A ⁻² ·s ⁻¹) [25]
J	Boundary current density (A·m ⁻²)	<i>β₁, β₂</i>	Dimensionless numbers (1.385)
<i>k</i>	Thermal conductivity (W·m ⁻¹ ·K ⁻¹)	<i>ε</i>	Thermal emissivity (0.8)
<i>k_B</i>	Boltzmann constant (1.38 × 10 ⁻²³ J·K ⁻¹)	<i>ε_n</i>	Net emission coefficient (W·m ⁻³ ·Sr ⁻¹)
<i>l_e</i>	Extension length of wire (0.012 m)	<i>ζ</i>	Stefan-Boltzmann constant (5.67 × 10 ⁻⁸ W·m ⁻² ·K ⁻⁴)
<i>m</i>	Droplet mass (kg)	<i>μ</i>	Dynamic viscosity (kg·m ⁻¹ ·s ⁻¹)
<i>M₁</i>	Relative mass of argon (kg·mol ⁻¹)	<i>μ₀</i>	Vacuum permeability (1.26 × 10 ⁻⁶ H·m ⁻¹)
<i>M₂</i>	Relative mass of iron vapor (kg·mol ⁻¹)	<i>μ₁</i>	Viscosity of argon (kg·m ⁻¹ ·s ⁻¹)
<i>p</i>	Pressure (Pa)	<i>μ₂</i>	Viscosity of iron vapor (kg·m ⁻¹ ·s ⁻¹)
<i>P_{atm}</i>	Atmospheric pressure (1.013 × 10 ⁵ Pa)	<i>ρ</i>	Density (kg·m ⁻³)
<i>P_{vap}</i>	Partial pressure of iron vapor (Pa)	<i>ρ₁</i>	Density of argon (kg·m ⁻³)
<i>Q</i>	Flow rate of shielding gas (20 L·min ⁻¹)	<i>ρ₂</i>	Density of iron vapor (kg·m ⁻³)
<i>R</i>	Gas constant (8.314 J·mol ⁻¹ ·K ⁻¹)	<i>ρ_g</i>	Density of plasma (kg·m ⁻³)
<i>r_{droplet}</i>	Radius of droplet (m)	<i>ρ_m</i>	Density of molten metal (7800 kg·m ⁻³)
<i>r_n</i>	Nozzle radius (7.5 × 10 ⁻³ m)	<i>σ_e</i>	Electrical conductivity (S·m ⁻¹)
<i>r_w</i>	Wire radius (6 × 10 ⁻⁴ m)	<i>σ</i>	Surface tension coefficient (1.2 N·m ⁻¹)
<i>S_E</i>	Electron migration heat (J·m ⁻³ ·s ⁻¹)	<i>φ</i>	Electric potential (V)

$$\frac{\partial(\rho v)}{\partial t} + \nabla \cdot (\rho v v) - \mu \nabla^2 v = -\nabla p + \rho g + F_{ST} + F_{em} \quad (3)$$

where the second-fifth terms of the right side represented gravity, surface tension force and electromagnetic force, respectively. The surface tension force was calculated by Eq. 4 [27].

$$\vec{F}_{ST} = -\sigma \nabla \cdot \left(\frac{\nabla F_m}{|\nabla F_m|} \right) \frac{\nabla F_m}{|\nabla F_m|} \quad (4)$$

(3) Energy conservation equation (Eq. 5)

$$\frac{\partial(\rho h)}{\partial t} + \nabla \cdot (\rho v h) = -\nabla \cdot \left(\frac{k}{C_p} \nabla h \right) + W + S_E - S_{Rg} - S_{Rl} \quad (5)$$

where the second-fifth terms of the right side represented the Joule heat generation, electron migration heat, liquid and gas phase radiation heat dissipation, respectively. They were calculated by Eq. 6–9.

$$W = \frac{j^2}{\sigma_e} \quad (6)$$

$$S_E = \frac{5k_B}{2e} j \nabla T \quad (7)$$

$$S_{Rg} = -\epsilon \zeta (T^4 - T_0^4) |\nabla F_m| \quad (8)$$

$$S_{RI} = -4\pi \epsilon_n \quad (9)$$

(4) Equations of electromagnetic field

The electromagnetic field was solved using the magnetic vector potential method. A User-Defined Scalar (UDS) transport equation was used to solve the current continuity equation (Eq. 10). The current density distribution was solved according to Ohm's law, as described in Eq. 11. Three UDS transport equations were used to solve the magnetic vector potential, where the current density was regarded as the source term, as described in Eq. 12. The magnetic flux density was the rotation of the magnetic vector potential, and then the electromagnetic force was solved using Fleming's Left Hand Rule, as described in Eq. 13–14.

$$\nabla \cdot (\sigma_e \nabla \varphi) = 0 \quad (10)$$

$$J = -\sigma_e \cdot \nabla \varphi \quad (11)$$

$$-\nabla^2 A_x = \mu_0 J_x; \quad -\nabla^2 A_y = \mu_0 J_y; \quad -\nabla^2 A_z = \mu_0 J_z \quad (12)$$

$$B = \nabla \times A \quad (13)$$

$$F_{emx} = J_y B_z - J_z B_y, \quad F_{emy} = J_z B_x - J_x B_z, \quad F_{emz} = J_x B_y - J_y B_x \quad (14)$$

(5) Volume of fluid equation (Eq. 15)

The free surface of droplet was reconstructed by the VOF equation [28].

$$\frac{\partial F}{\partial t} + (\nabla \cdot vF) = \frac{S_m}{\rho} \quad (15)$$

F was the volume fraction of metal phase in the grid. $F = 1$ indicated that the grid was filled with metal; $F = 0$ indicated that the grid was filled with argon; $0 < F < 1$ indicated that the grid contained both metal and argon.

2.3 Iron vapor

A UDS equation was used to calculate the iron vapor diffusion, as described in Eq. 16. The two terms on the left side was the transient term and convection term, and on the right side was the diffusion term and iron vapor source term. The diffusion coefficient (D) was calculated according to Eq. 17 [29, 30].

$$\frac{\partial(\rho Y_m)}{\partial t} + \nabla \cdot (\rho \vec{v} Y_m) = \nabla \cdot (\rho D \nabla Y_m) \quad (16)$$

$$D = \frac{2\sqrt{2}(1/M_1 + 1/M_2)}{[(\rho_1^2/\beta_1^2\mu_1^2M_1)^{0.25} + (\rho_2^2/\beta_2^2\mu_2^2M_2)^{0.25}]^2} \quad (17)$$

L, L, Wang [12] et al. found that the metal vapor generated by the droplet surface was much more than that generated by the weld pool surface, which was neglected in this mode. The iron vapor generated by the droplet was calculated according to Eq. 18 [19]. P_{vap} was the partial pressure of iron vapor, which was calculated according to Eq. 19.

$$Y_m = \frac{P_{vap}M_1}{P_{vap}M_1 + (P_{atm} - P_{vap})M_2} \quad (18)$$

$$P_{vap} = P_{atm} \left(\frac{-H_{vap}}{R} \left(\frac{1}{T_1} - \frac{1}{T_b} \right) \right) \quad (19)$$

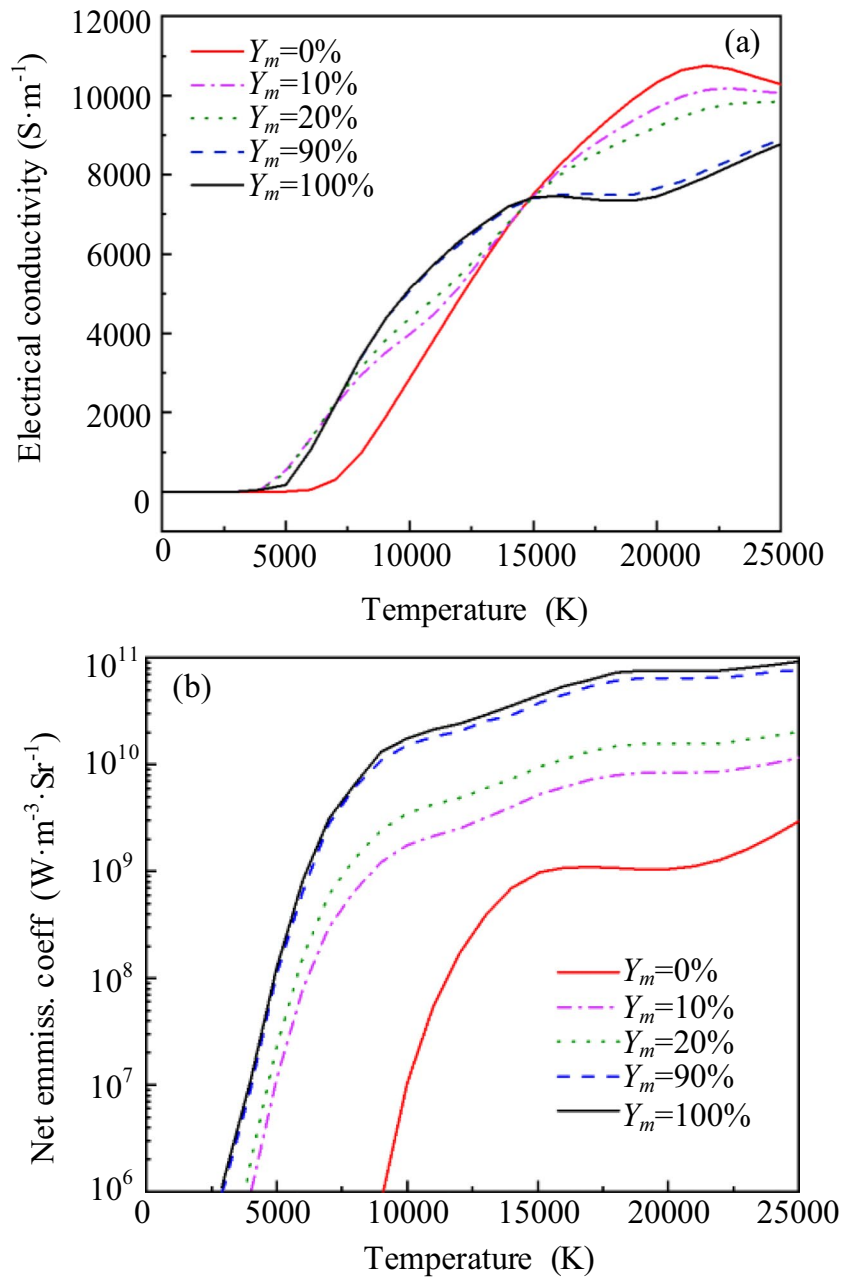
The iron vapor generated on the surface of the droplet diffused in the arc, which changed the physical properties of the plasma. Murphy [19] et al. found that the electrical conductivity and net radiation coefficient were sensitive to the Y_m , as shown in Fig. 1. In order to improve the convergence without affecting the calculation accuracy, when the temperature was below 4000 K, the conductivity was set to 0.03 S/m, which did not change with the iron vapor content and temperature. The other physical properties of the plasma were only set as functions of temperature.

2.4 Boundary conditions

The calculation zone was shown in Fig. 2, which did not include the solid wire entities or grids, but only considered its fixed side and tip faces. The shielding gas flowed in from area 1, and the velocity distribution in the oxy plane was calculated by Eq. 20 [7]. The welding current flowed in from the wire tip (Area 2), and the current density was calculated by Eq. 21. The boundary condition at Area 2 was set as the inlet of the metal phase velocity, the volume fraction of the metal phase was 100%, and the temperature was 1800 K. The droplet outflow velocity, that was, the wire feeding rate, was related to the welding current (I) and the length of the wire extension (l_e), the velocity distribution was calculated by 22 [31, 32]. Area 3 was the pressure outlet. The rectangle (ABCD) was the workpiece surface. The specific boundary condition settings were listed in Table 2.

$$v_{gas} = \frac{2Q}{\pi} \frac{\{r_n^2 - (x^2 + y^2) + (r_n^2 - r_w^2) \frac{\ln(\sqrt{x^2+y^2}/r_n)}{\ln(r_n/r_w)}\}}{\{r_n^4 - r_w^4 + \frac{(r_n^2 - r_w^2)^2}{\ln(r_n/r_w)}\}} + v_w \frac{\ln \frac{r_n}{\sqrt{x^2+y^2}}}{\ln \frac{r_n}{r_w}} \quad (20)$$

Fig. 1 Gas phase thermos-physical parameters: (a) electrical conductivity and (b) net emission coefficient



$$j = I / \pi r_w^2 \tag{21}$$

$$v_w = \alpha I + \beta I_e I^2 \tag{22}$$

2.5 Materials

In this model, the diameter of the wire was 1.2 mm, and the shielding gas was pure argon. The temperature-dependent physical properties of the shielding gas were used, and they were referenced from Murphy [19]. The wire of model was

mild steel (Q235). Its detailed thermo-physical properties were listed in Table 3[7, 24].

3 Results and discussion

The welding parameters used in the model were given in Table 1. The changes of the average temperature and the iron vapor mass fraction of the grid with welding time were shown in Fig. 3. The average temperature decreased rapidly during 0–2 ms, and then stabilized at about 1900 K at

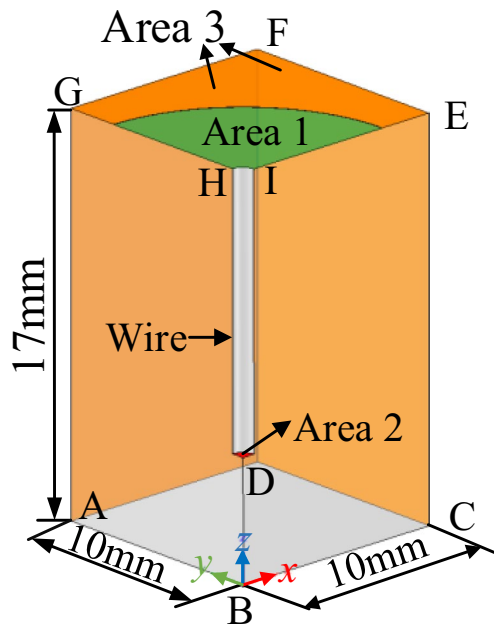


Fig. 2 GMAW arc-droplet three-dimensional model

5.0 ms. The Y_m increased rapidly during 0–5 ms, then grew slowly during 5–10 ms, which was mainly due to the iron vapor accumulation in the surroundings and had little effect on the arc column. Compared with the arc shape captured by high-speed camera, it was reasonable to consider that the simulated arc plasma reached quasi-steady state at 5ms. According to the arc shape and temperature distribution, 5000 K isotherm was defined as the arc edge, the zone with temperature between 5000–7000 K was defined as the arc periphery, and the zone with temperature higher than 7000 K was defined as the arc inner layer.

3.1 Distribution of iron vapor

The distribution of iron vapor in the arc plasma was shown in Fig. 4. Equation 14 indicated that the distribution of iron vapor was related to both convection and diffusion. The plasma moved downward at high velocity along the z -axis, so the transport rate of iron vapor along the axial direction

was faster than that in the radial direction, and its distribution was like a bell.

At 5.0 ms, Y_m was higher than 15% around the forming droplet, within the range of no more than 0.5 mm from the droplet surface, as shown in Fig. 4(a). Y_m in the inner layer of the arc was higher than 10%, with a distribution radius of 2.0 mm. Y_m in the arc periphery was lower than 10%. At 6.6 ms, the first droplet was separated from the wire tip, Y_m around the first droplet was over 20%, Y_m in the inner layer increased to 15%, while it hardly increased in the arc periphery, as shown in Fig. 4(b). At 7.8 ms, as the first droplet passing through the arc column, Y_m around it was up to 25%, and an iron-rich channel, with Y_m values over 20% and a radius of 1.0 mm, was formed in the inner layer of the arc, as shown in Fig. 4(c).

The droplet transfer had little effect on the iron vapor distribution in arc periphery but increased the Y_m of the arc inner layer. It could affect the electrical conductivity and net emission coefficient of the plasma, and then change the current density and temperature distribution.

3.2 Current density distribution

Figure 5 illustrates the electrical conductivity distribution. Figure 6 illustrates the current density distribution. Their distributions in space were similar, that was, where the conductivity was high, the current density was larger. The current flow from the anode (wire tip) to the cathode (workpiece). As the conductivity of iron was much higher than that of plasma, and the current was continuous, the current density was perpendicular to the gas–liquid interface near the anode, and perpendicular to the workpiece surface near the cathode. Due to the "tip effect" and "skin effect", the current density at the wire tip was significantly larger than that on the workpiece surface.

Table 3 Physical properties of mild steel

Density [kg/m ³]	7860
Viscosity [Pa·s]	6 × 10 ⁻³
Surface tension [N/m]	1.2
Electrical conductivity [S/m]	7.7 × 10 ⁵
Specific heat [J·kg ⁻¹ ·K ⁻¹]	695–800

Table 2 Setting of boundary conditions

Boundary	T (K)	v (m/s)	$\phi\phi$ (V)	A (Wb/m ²)	Y_m
ABCD	2000	0	0	$\frac{\partial A}{\partial n} = 0$	$\frac{\partial Y_m}{\partial n} = 0$
Area1	400	v_{gas}	$\frac{\partial \phi}{\partial n} = 0$	$\frac{\partial A}{\partial n} = 0$	0
Area2	1800	v_w	$\frac{\partial \phi}{\partial n} = j$	$\frac{\partial A}{\partial n} = 0$	$\frac{\partial Y_m}{\partial n} = 0$
Area3	1000	Pressure outlet	$\frac{\partial \phi}{\partial n} = 0$	0	0
Wire	$T_w = 1800 - [1400 \times (z - 0.005)]$	0	$\frac{\partial \phi}{\partial n} = 0$	0	$\frac{\partial Y_m}{\partial n} = 0$

At 5.0 ms, iron-rich channel had not been formed, and the plasma conductivity was mainly determined by temperature. The conductivity around the forming droplet was up to 8000 s/m, and it was about 2500 s/m in the arc inner layer, as shown in Fig. 5(a). The current density around the

forming droplet was up to 3×10^7 A/m², and it was about 4×10^6 A/m² in the arc inner layer, as shown in Fig. 6(a). At 6.6 ms, as the iron vapor accumulated, the temperature around the first droplet would decrease, and the conductivity reduced to 3500 s/m. The current density decreased to

Fig. 3 Grid average temperature and iron vapor mass fraction

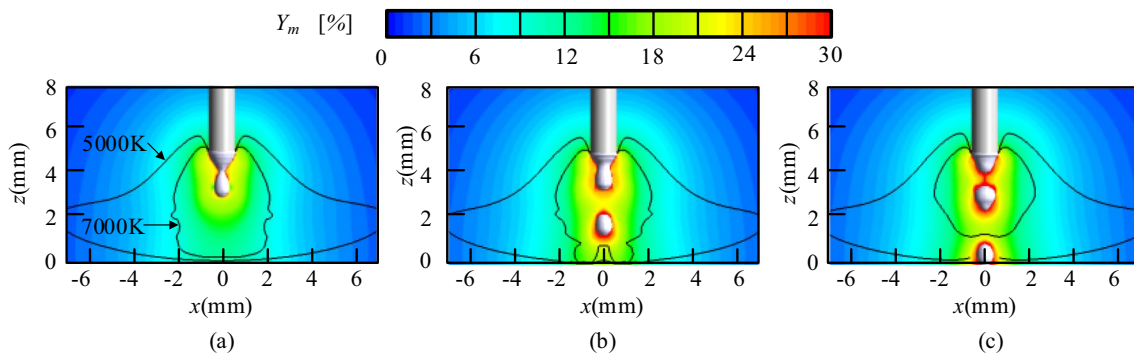
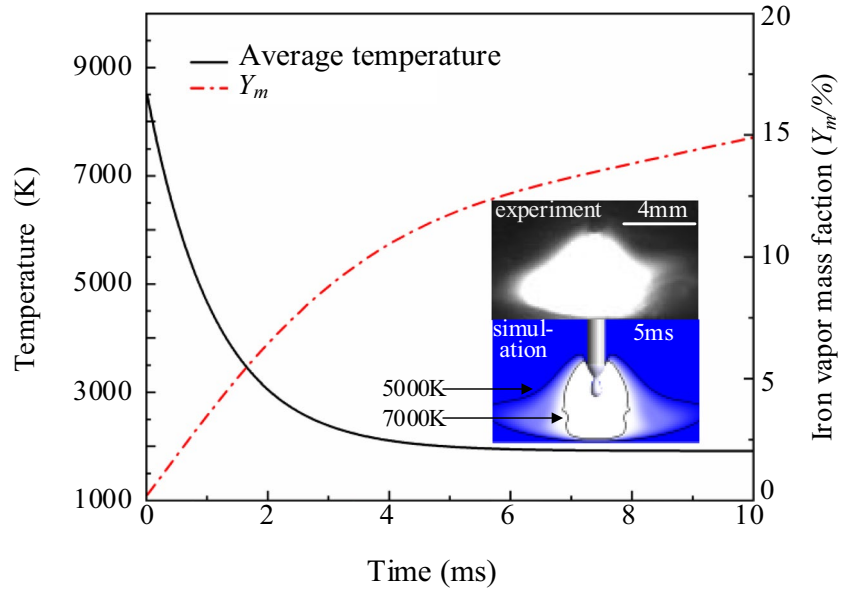


Fig. 4 Distribution of iron vapor in arc at different time: (a) $t=5.0$ ms, (b) $t=6.6$ ms and (c) $t=7.8$ ms

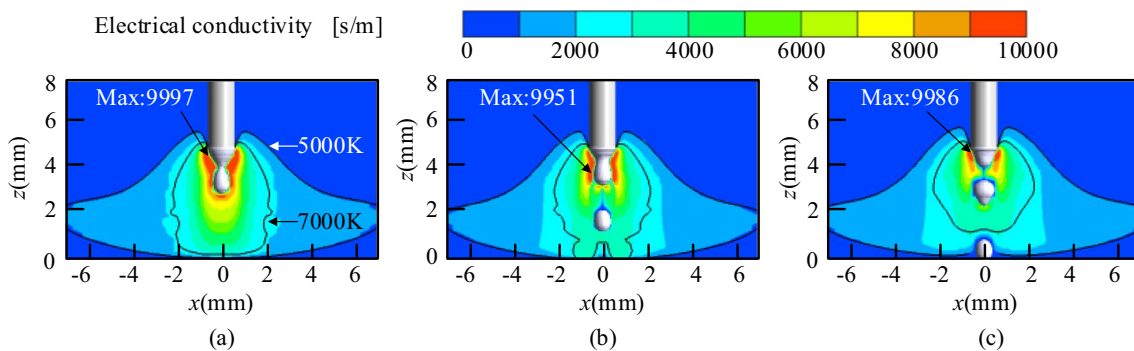


Fig. 5 Distribution of electrical conductivity: (a) $t=5.0$ ms, (b) $t=6.6$ ms and (c) $t=7.8$ ms

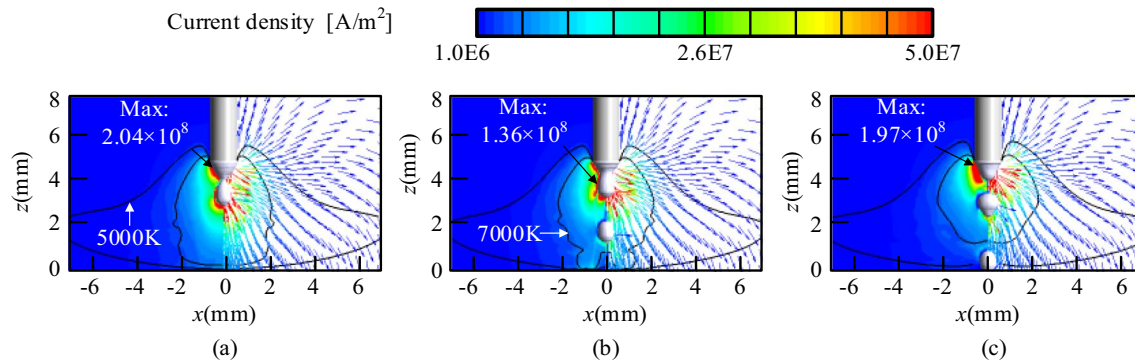


Fig. 6 Distribution of current density in the arc: (a) $t=5.0$ ms, (b) $t=6.6$ ms and (c) $t=7.8$ ms

6×10^6 A/m². In the upper part of arc inner layer, the conductivity and current density were still large. In the lower part, they were decreased obviously, as shown in Fig. 5(b) and 6(b). At 7.8 ms, the conductivity around the first droplet decreased to 2000s/m, and the current density was as low as 4×10^6 A/m². In the lower part of arc inner layer, the conductivity and current density further decreased, as shown in Fig. 5(c) and 6(c).

The droplet transfer had little effect on the electrical conductivity and the current density distribution in the arc periphery but formed a low electrical conductivity and current density channel in the arc inner layer. It could affect the Joule heat generation, electromagnetic force, and arc pressure, and then change the arc thermal-pressure distribution and droplet behavior.

The workpiece in this model was simplified as a surface, so the current density distribution on the plane $z = 1$ mm was selected to understand that on the workpiece surface, as shown in Fig. 7. As the droplet passed through the arc column, the current density in the arc inner layer decreased, that was, the radius of contour line with a value of 3.7×10^6 A/m² shrank from 1.8 mm to 1.1 mm. While there was almost no change in the arc periphery. From the point of view of time average, the

current density still presented a Gaussian distribution, with a peak value of 1×10^7 A/m² and a distribution radius of 6.0 mm. It could provide a reference and basis for fluid–solid–heat coupling numerical simulation of weld pool behavior and bead formation.

3.3 Arc heat and force

3.3.1 Temperature Distribution

The temperature field was the result of a balance among Joule heat, electron migration heat and radiation, as shown in Fig. 8. The Joule heat generation was proportional to the square of current density and inversely proportional to electrical conductivity. Radiation was the heat dissipation from the high temperature plasma, which was proportional to the net emission coefficient. Electron migration heat was proportional to the current density and temperature gradient, which was caused by the directionally movement of electrons with different kinetic energy from cathode to anode driven by the electric field. When the direction of current density was consistent with that of temperature gradient, it was positive, that was, heat generation. On the contrary, it was negative, that was, heat dissipation.

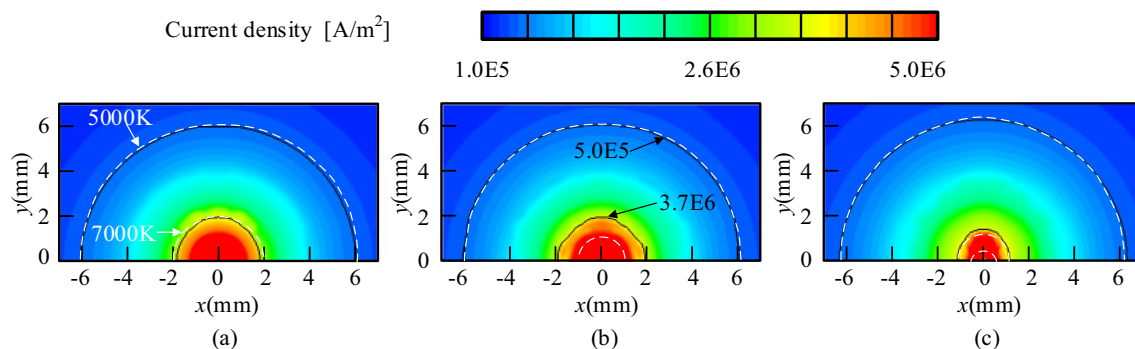


Fig. 7 Current density distribution on workpiece surface: (a) $t=5.0$ ms, (b) $t=6.6$ ms and (c) $t=7.8$ ms

At 5.0 ms, the current density around the forming droplet was higher than $3 \times 10^7 \text{ A/m}^2$, and the joule heat generation was up to $1 \times 10^{11} \text{ J}\cdot\text{m}^{-3}\cdot\text{s}^{-1}$. The current density of the arc inner layer was higher than $4 \times 10^6 \text{ A/m}^2$, and the joule heat generation was higher than $8 \times 10^9 \text{ J}\cdot\text{m}^{-3}\cdot\text{s}^{-1}$, as shown in Fig. 8(a). Around the forming droplet, the net emission coefficient was about $8 \times 10^9 \text{ W}\cdot\text{m}^{-3}\cdot\text{Sr}^{-1}$. The radiation was higher than $1 \times 10^{11} \text{ J}\cdot\text{m}^{-3}\cdot\text{s}^{-1}$. The net emission coefficient in the arc inner layer was about $1 \times 10^9 \text{ W}\cdot\text{m}^{-3}\cdot\text{Sr}^{-1}$. The radiation was about $1 \times 10^{10} \text{ J}\cdot\text{m}^{-3}\cdot\text{s}^{-1}$, as shown in Fig. 8(b).

Electron migration resulted in heat generation only near the droplet surface up to $1 \times 10^{12} \text{ J}\cdot\text{m}^{-3}\cdot\text{s}^{-1}$. In other areas of the arc, electron migration led to heat dissipation. It was as high as $-1 \times 10^{10} \text{ J}\cdot\text{m}^{-3}\cdot\text{s}^{-1}$ around the forming droplet. It rapidly reduced to $-1 \times 10^8 \text{ J}\cdot\text{m}^{-3}\cdot\text{s}^{-1}$ in the arc inner layer and $-1 \times 10^7 \text{ J}\cdot\text{m}^{-3}\cdot\text{s}^{-1}$ at the arc edge, as shown in Fig. 8(c).

At 6.6 ms, the first droplet was separated from the wire tip, and the current density around it significantly decreased to $6 \times 10^6 \text{ A/m}^2$, which led to a reduction of the Joule heat to $1 \times 10^{10} \text{ J}\cdot\text{m}^{-3}\cdot\text{s}^{-1}$. In the upper part of arc inner layer, the

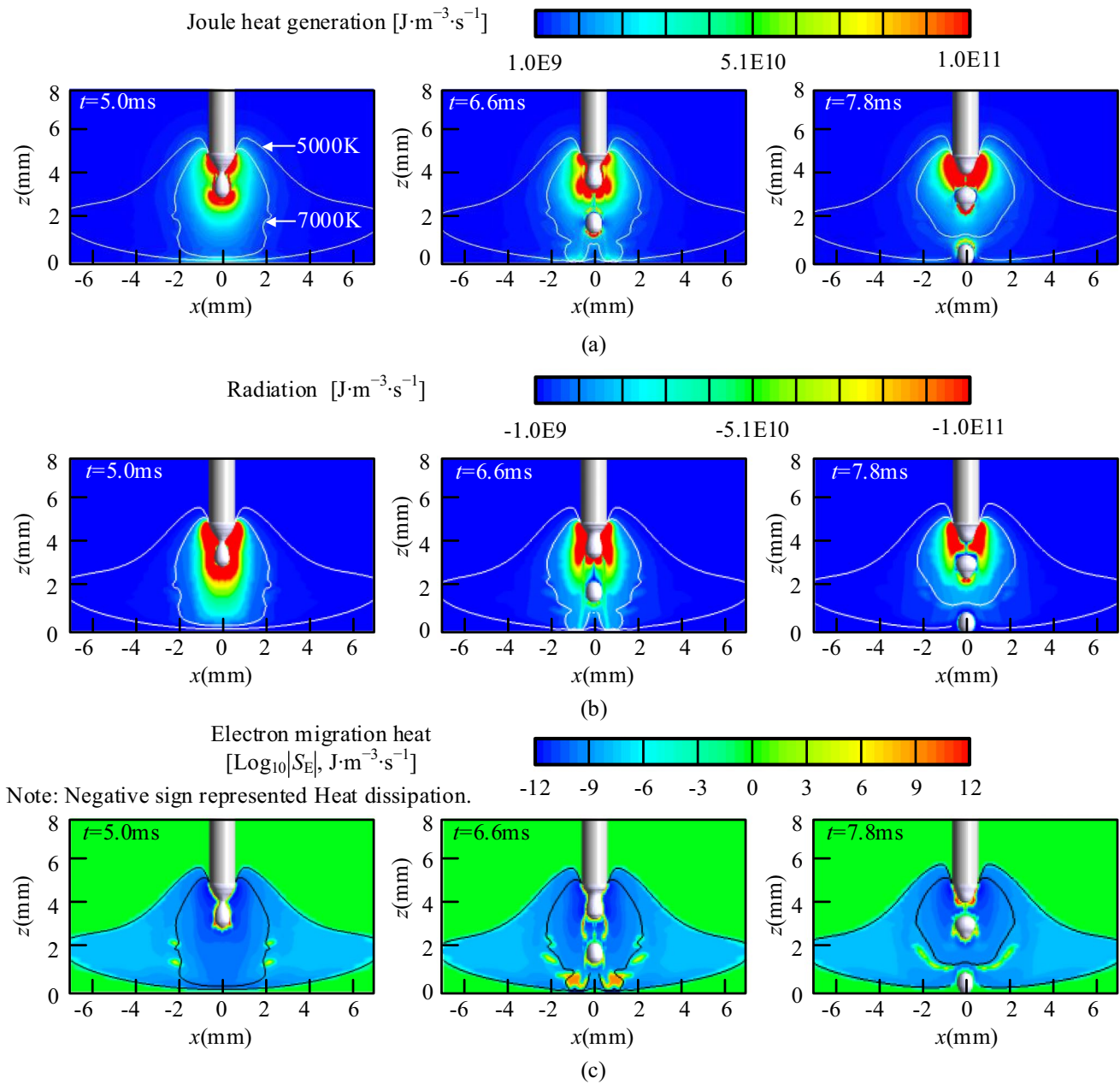


Fig. 8 Heat generation and dissipation in the arc: (a) Joule heat (b) radiation heat dissipation and (c) electron migration heat

Joule heat was still large. In the lower part, it was decreased obviously, as shown in Fig. 8(a). Around the first droplet, the increase of Y_m was not enough to change the fact that the net radiation coefficient decreased to $2 \times 10^9 \text{ W}\cdot\text{m}^{-3}\cdot\text{Sr}^{-1}$ due to temperature reduction, so the radiation heat dissipation decreased to $2.5 \times 10^{10} \text{ J}\cdot\text{m}^{-3}\cdot\text{s}^{-1}$. In the upper part of arc inner layer, the radiation was still strong. In the lower part, it was weakened obviously, as shown in Fig. 8(b). The electron migration heat upper the first droplet surface was negative, below it was positive. The decrease of current density and temperature gradient reduced the electron migration dissipation around the droplet to $-1 \times 10^9 \text{ J}\cdot\text{m}^{-3}\cdot\text{s}^{-1}$. In the arc inner layer, the electron migration heat generation near the wire tip was up to $1 \times 10^{12} \text{ J}\cdot\text{m}^{-3}\cdot\text{s}^{-1}$. In the upper part, the electron migration dissipation was as high as $-1 \times 10^{10} \text{ J}\cdot\text{m}^{-3}\cdot\text{s}^{-1}$, and it was decreased to $-1 \times 10^9 \text{ J}\cdot\text{m}^{-3}\cdot\text{s}^{-1}$ at the lower part, as shown in Fig. 8(c).

At 7.8 ms, the current density around the first droplet further decreased to $4 \times 10^6 \text{ A/m}^2$, and the conductivity reduced to 2000s/m, which kept the Joule heat generation at $1 \times 10^{10} \text{ J}\cdot\text{m}^{-3}\cdot\text{s}^{-1}$. In the arc inner layer, Joule heat was concentrated in the upper part, as shown in Fig. 8(a). Around the first droplet, the net radiation coefficient decreased to $1 \times 10^9 \text{ W}\cdot\text{m}^{-3}\cdot\text{Sr}^{-1}$ due to temperature reduction, so the radiation heat dissipation decreased to $1 \times 10^{10} \text{ J}\cdot\text{m}^{-3}\cdot\text{s}^{-1}$. In the arc inner layer, the radiation heat dissipation was concentrated in the upper part, as shown in Fig. 8(b). Electron migration generated heat at the wire tip. In other areas of the arc, electron migration led to heat dissipation. It reduced to $-1 \times 10^8 \text{ J}\cdot\text{m}^{-3}\cdot\text{s}^{-1}$ around the droplet, as shown in Fig. 8(c).

Joule heat and thermal radiation had a wide range of effects, and their integrals in the arc space were $900 (\pm 100) \text{ J}\cdot\text{m}^{-3}\cdot\text{s}^{-1}$ and $-600 (\pm 50) \text{ J}\cdot\text{m}^{-3}\cdot\text{s}^{-1}$, respectively, which played a leading role in the overall heat balance of the arc space. The electron migration heat mainly acted on the upper part of arc inner layer. The heat generation on the surface of the wire tip was much greater than the heat dissipation in

other areas, and its integral in the arc space was about $400 (\pm 50) \text{ J}\cdot\text{m}^{-3}\cdot\text{s}^{-1}$. During the droplet transfer, the Joule heat around the first droplet decreased significantly due to the rapid drop of current density. However, with the increase of Y_m , the radiation dissipation decreased relatively slowly. A channel with sharp fluctuations in energy density was formed along the path of droplet, which would significantly affect the temperature field in the arc inner layer.

Figure 9 shows the temperature distribution of the symmetry plane. The temperature distribution in the arc periphery remained stable, while it changed dramatically in the arc inner layer as the droplet passing through the arc column.

At 5.0 ms, around the forming droplet, the Joule heat generation and radiation heat dissipation could offset each other in numerical value. The electron migration heat only near the droplet surface was positive, and then quickly became negative. The plasma temperature near the droplet surface was as high as 20,000 K, and then rapidly decreased to 15,000 K. In the upper part of arc inner layer, the Joule heat generation was larger than the radiation heat dissipation. While, the heat dissipation caused by electron migration was so strong that the temperature decreased rapidly, showing a spherical shape. In the lower part, the influence of electron migration was weak, and the Joule heat generation was smaller than the radiation heat dissipation. The temperature gradient decreased, and showed a cylindrical shape with a radius of about 2 mm. In the arc periphery, the electron migration heat could be neglected, and the Joule heat generation was slightly stronger than the radiation heat dissipation. The plasma reached a thermal equilibrium state under the heat convection of the cold shielding gas, and presented a trumpet shape, as shown in Fig. 9(a). At 6.6 ms, around the first droplet, the radiation heat dissipation was much stronger than Joule heat generation. Meanwhile, electron migration resulted in heat dissipation. The plasma temperature rapidly decreased from 10000 K to 8000 K. In the upper part of arc inner layer, its thermal state remained unchanged and it kept a spherical shape. In the lower part, Joule heat decreased

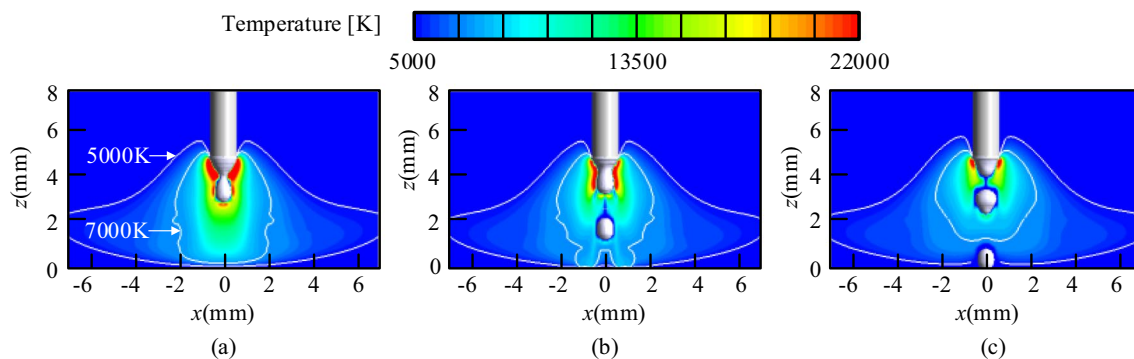


Fig. 9 Distribution of arc temperature: (a) $t = 5.0$ ms, (b) $t = 6.6$ ms and (c) $t = 7.8$ ms

significantly, leading to the shrinkage of the boundary of arc inner layer, as shown in Fig. 9(b). At 7.8 ms, around the first droplet, the Joule heat generation and radiation heat dissipation could offset each other in numerical value. The electron migration heat was negligible. A low temperature zone with a temperature of about 7000 K was formed around the first droplet, and the inner layer of the arc shrinks into a sphere, as shown in Fig. 9(c).

The droplet transfer had little effect on the temperature distribution in the arc periphery. In the arc inner layer, the iron vapor emitted from the droplet surface enhanced the thermal radiation, breaking the balance between heat generation and dissipation, thus forming a low temperature channel.

The temperature distribution on the plane $z = 1$ mm was selected to understand that on the workpiece surface, as shown in Fig. 10. As the droplet passed through the arc column, the temperature in the arc inner layer decreased, that was, the radius of contour line with a value of 7000 K shrank from 2.0 mm to 1.0 mm. While there was almost no change in the arc periphery. From the point of view of time average, the temperature still presented a Gaussian distribution. It could provide a reference and basis for solid-heat coupling numerical simulation of weld joint stress and strain.

3.3.2 Electromagnetic force

During the welding process, an electrical circuit was formed between the wire (anode) and the workpiece (cathode), and the induced magnetic field was generated in the arc space. The moving charged particles was subjected to Lorentzian force in the magnetic field, that was, electromagnetic force, which was divided into axial and radial directions, as shown in Fig. 11.

At 5.0 ms, there were big radial current components at the wire tip and droplet sides, respectively, as shown in Fig. 6. The former induced an axial electromagnetic force up to -4×10^6 N/m³ above the forming droplet, as shown in Fig. 11. Its negative sign indicated the opposite direction

of the z -axis, that was, from the wire tip to the workpiece surface. It accelerated the downward flow of the plasma and promoted the droplet to be separated from the wire tip. The latter induced an axial electromagnetic force up to 2×10^6 N/m³ at the droplet sides. It exerted an upward force on the droplet and hindered the droplet transfer. The axial electromagnetic force in the arc inner layer decreased rapidly to -7.6×10^3 N/m³, and it was smaller than -5×10^3 N/m³ at the arc edge. Figure 11(b) shows the distribution of radial electromagnetic force. It reached -4.0×10^6 N/m³ at the necking, as the big axial current component. Its negative sign indicated axial contraction, that was, from the arc periphery to the arc center. It acted as a shear force at the forming droplet, leading to necking, thus promoting the droplet transfer. The radial electromagnetic force in the upper part of arc inner layer was about -1.5×10^5 N/m³, and it in the lower part decreased to -3.0×10^4 N/m³. It was only -5×10^3 N/m³ in the arc periphery.

At 6.6ms, the current density around the first droplet decreased 80%. The electromagnetic force along the axial direction decreased to 3.3×10^5 N/m³, and that along the radial direction decreased to -8×10^5 N/m³. There was always a downward electromagnetic force in the arc inner layer, which was mainly concentrated in the upper part, and had little change during droplet transfer. The radial electromagnetic force in the arc inner layer increased, which was a factor for the shrinkage of the arc inner layer. At 7.8ms, electromagnetic force around the first droplet along the axial and radial directions were 2.8×10^5 N/m³ and -5×10^5 N/m³, respectively. It intensified the shrinkage of the arc inner layer.

The integrals of electromagnetic force along the axial and radial directions were $-(96 \pm 4) \times 10^{-4}$ N and $-(15.2 \pm 4) \times 10^{-4}$ N, respectively. Both fluctuated periodically with droplet transfer. The downward axial electromagnetic force caused high-speed plasma flow. On the one hand, it generated a viscous drag force to promote the droplet transfer. On the other hand, it intensified the impingement of particles on the weld pool and increased

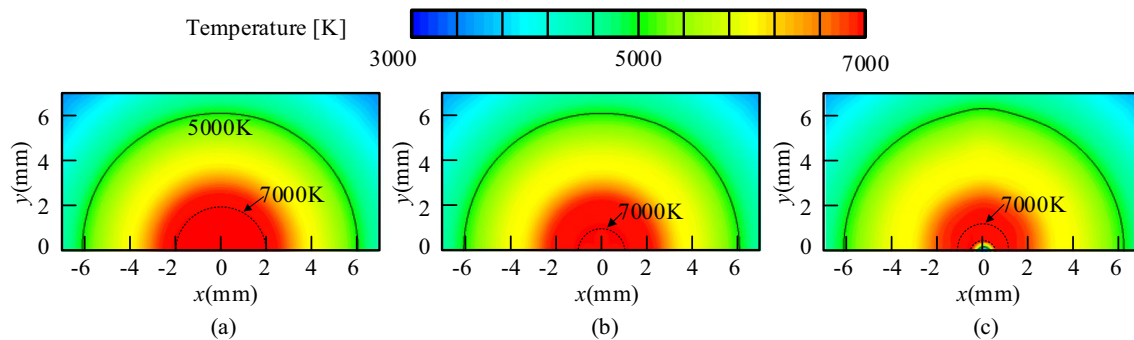


Fig. 10 Arc temperature distribution on workpiece surface: (a) $t = 5.0$ ms, (b) $t = 6.6$ ms and $t = 7.8$ ms

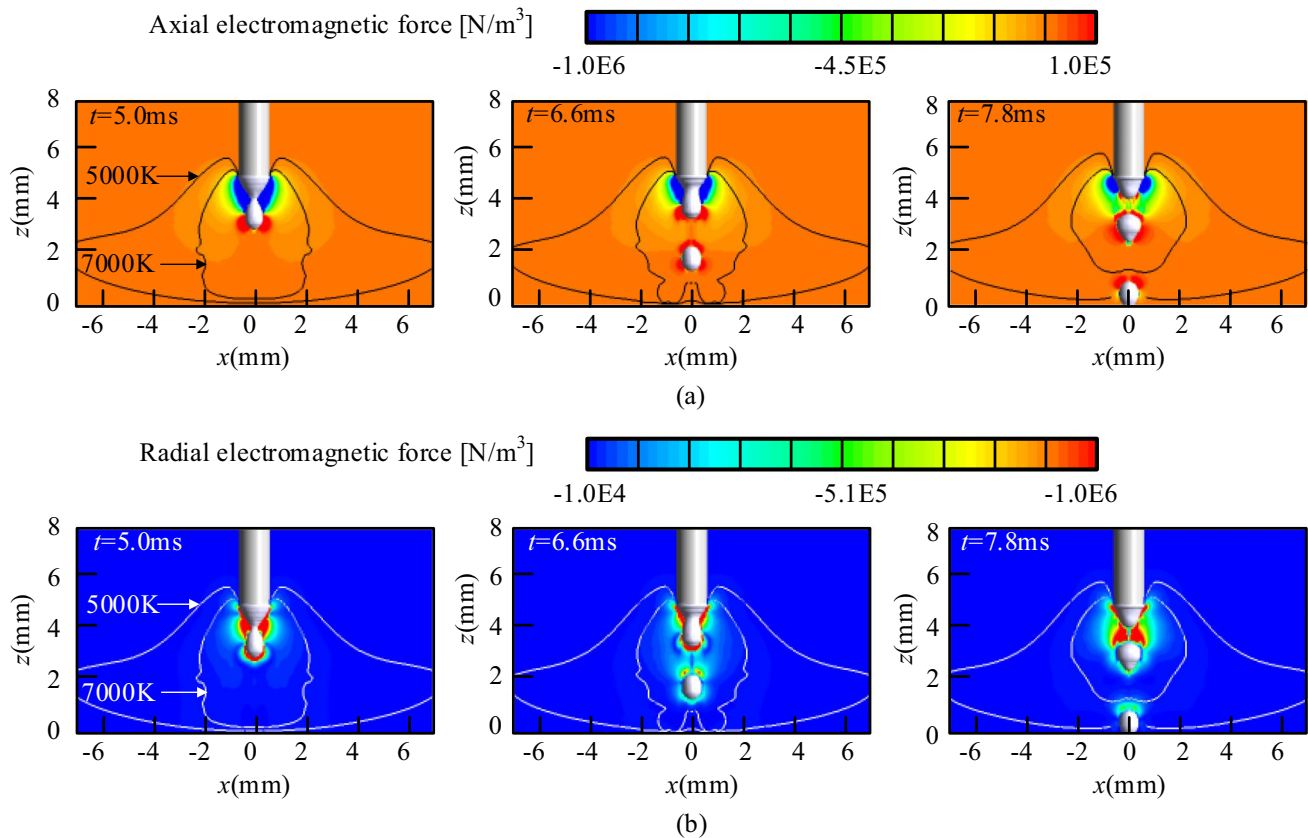


Fig. 11 Electromagnetic force distribution: (a) Axial direction and (b) Radial direction

the dynamic pressure of the arc. The radial electromagnetic force constrained the plasma to a trumpet shape. On the one hand, it promoted the formation of necking, which was conducive to droplet transfer. On the other hand, it generated a pressure difference along the axial direction and created a static pressure on weld pool.

3.3.3 Arc pressure

The arc pressure could be divided into dynamic pressure and static pressure. The dynamic pressure was proportional to the square of the plasma velocity, which was affected by the axial electromagnetic force and static pressure difference. The static pressure, on the one hand, was converted from the kinetic energy of high velocity plasma, and on the other hand, was induced by the compression of radial electromagnetic force.

At 5.0 ms, the plasma velocity exceeded 300 m/s under the acceleration of axial electromagnetic force in the upper part of arc inner layer. Then it was blocked by the workpiece,

and gradually decelerated in the lower part of arc inner layer, as shown in Fig. 12 (a). The distribution of arc dynamic pressure was very similar to that of plasma velocity, as shown in Fig. 13(a). It reached a peak value of 500 Pa at the sides of droplet, and then reduced to zero on the work piece surface. Due to the continuity of the plasma flow, the velocity below the droplet was very small, resulting in a low-pressure zone, and the dynamic pressure distribution was generally cylindrical. The kinetic energy of the plasma was converted into static pressure, forming a mountain like high-pressure zone with a peak value of 450 Pa above the workpiece surface, as shown in Fig. 13(b). At the necking, the radial electromagnetic force was so strong that a static pressure with a peak value of 2000 Pa appeared. Below the forming droplet, there was neither energy conversion nor electromagnetic compression, forming a low-pressure zone. The static pressure was dumbbell shaped along the axial direction, larger at both ends and smaller in the middle, which in turn affected the velocity distribution of the plasma to a certain extent.

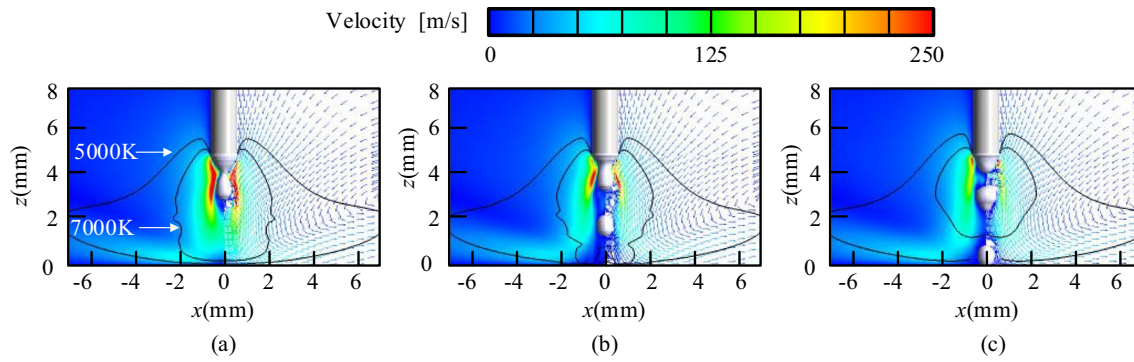


Fig. 12 Distribution of velocity field: (a) $t=5.0$ ms, (b) $t=6.6$ ms and (c) $t=7.8$ ms

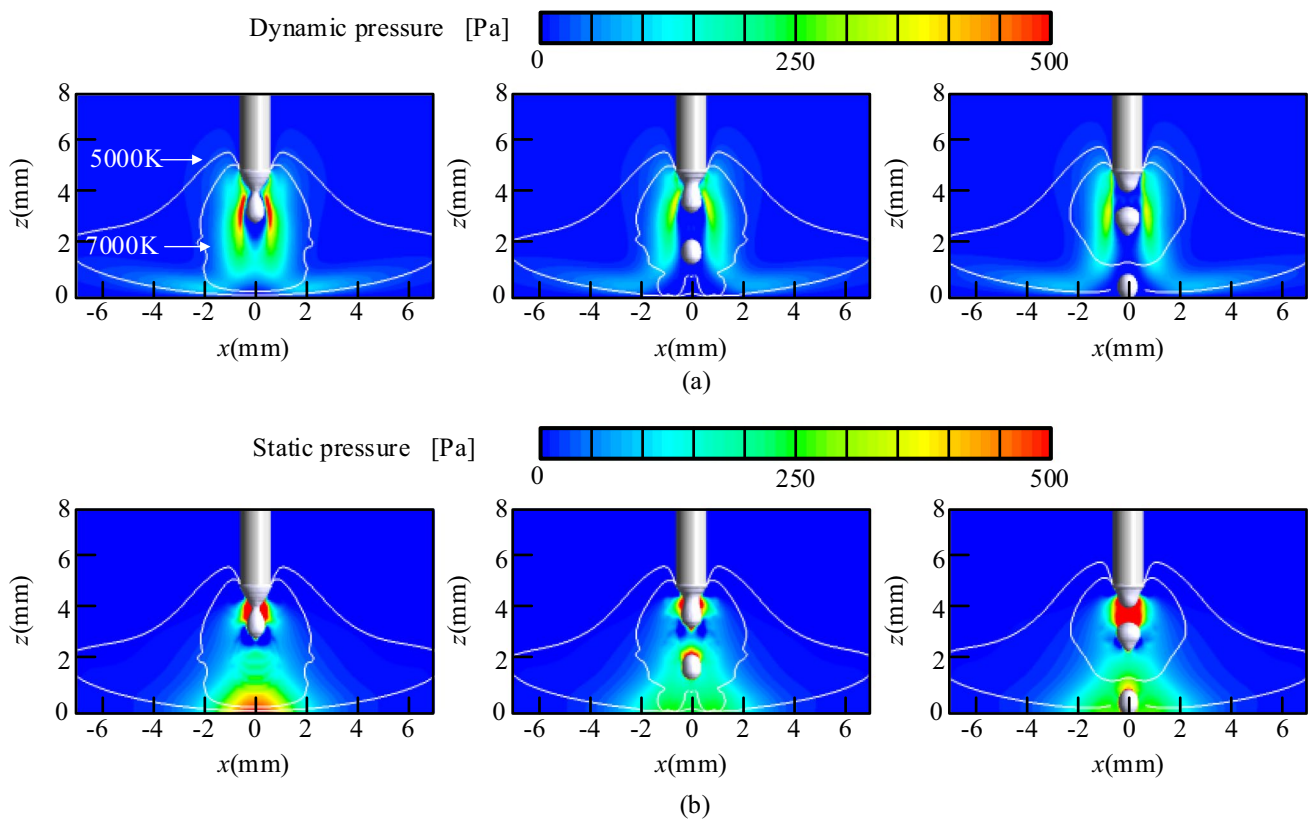


Fig. 13 Distribution of arc pressure: (a) dynamic pressure and (b) static pressure

At 6.6 ms, the weakening of the axial electromagnetic force made the plasma velocity in the upper part of arc inner layer decrease to 200 m/s. The droplet blocked the continuity of the plasma flow, resulting in a low velocity zone between the first droplet and wire tip, as shown in Fig. 12 (b). The peak value of dynamic pressure decreased to 250 Pa, and a low-pressure zone corresponding to the low velocity zone appeared, as shown in Fig. 13(a). The impingement of plasma on the workpiece was weakened, and the static pressure above the workpiece was decreased, with a peak value

of only 300 Pa, as shown in Fig. 13(b). At the necking, the reduction of the radial electromagnetic force decreased the static pressure to 500 Pa, which weakened the axial acceleration of the plasma.

At 7.8 ms, the first droplet contacted the workpiece, and a low velocity channel for plasma flow formed on the path of droplet transfer, as shown in Fig. 12(c). Correspondingly, a low-pressure channel appeared, and the peak value of dynamic pressure decreased to 200 Pa, as shown in Fig. 13(a). The strong radial electromagnetic force at the

wire tip generated a static pressure with a peak value of 1100 Pa, as shown in Fig. 13(b). This high static pressure exerted a downward force on the second droplet to accelerate it, but had little effect on the axial acceleration of the plasma.

The dynamic arc pressure was mainly distributed in the inner arc layer, which changed from the initial cylindrical shape to the sleeve shape with low central pressure. The static arc pressure at the wire tip was dominated by radial electromagnetic force, which could promote necking and accelerate droplet. While it above the workpiece was dominated by the kinetic energy of plasma and distributed in a mountain shape. The arc pressure was an important factor affecting droplet transfer and weld pool behavior.

The total arc pressure distribution on the plane $z = 1$ mm was selected to understand that on the workpiece surface, as shown in Fig. 14. Its Gauss distribution verified that the dynamic pressure was converted to static pressure above the workpiece. As the droplet passed through the arc column, the pressure in the arc inner layer decreased, while it remained unchanged in the arc periphery. The shrinkage of the arc inner layer had little effect on the high-pressure zone, that was, the radius of contour line with a value of 140 Pa had not changed. The main reason was that the continuity of plasma flow made the change of velocity field not as rapid as that of current. The arc pressure could deform the surface of the weld pool and drove the metal flow, which was an important factor affecting weld pool behavior and bead formation [33–35].

3.4 Droplet transfer

The size, velocity and frequency of the droplet directly affected the behaviors of the weld pool, bead formation and welding quality [30]. The simulated droplet diameter was 0.8 mm, the impinging velocity was 1.3 m/s, and the transfer frequency was 454 Hz. The error with the experimental results was less than 9%, which verified the accuracy of the model [36, 37].

3.4.1 Forces acting on droplets

As shown in Fig. 15, under the action of gravity, surface tension, total electromagnetic force (F_{emz}), electromagnetic pinch force (generated by F_{emx} and F_{emy}) and plasma drag force, the droplet grew up, formed necking, separated from the wire tip, and finally impinged into the weld pool. To facilitate the analysis, the droplet transfer was divided into three stages: before necking, necking to separating, and after separating. For the first droplet, the critical points were 4.0 ms and 5.2 ms, as shown in Fig. 16.

(1) Gravity

In flat welding, the gravity was consistent with the moving direction of the droplet and promoted the droplet transfer. It could be calculated according to Eq. 23. Before necking, V was the volume of molten metal at the wire tip. After necking, V was the volume of molten metal below the necking, as shown in Fig. 15. After separating, V was the volume of droplet.

$$F_g = \rho g V \quad (23)$$

Before necking, F_g increased continuously. At 2.0 ms, F_g was 1.9×10^{-5} N. At 4.0 ms, the gravity of the molten metal at wire tip reached 3.4×10^{-5} N, while that below the necking (F_g) was only 0.7×10^{-5} N. After necking, F_g continued to increase again, and reached 1.4×10^{-5} N at 5.2 ms.

(2) Surface tension

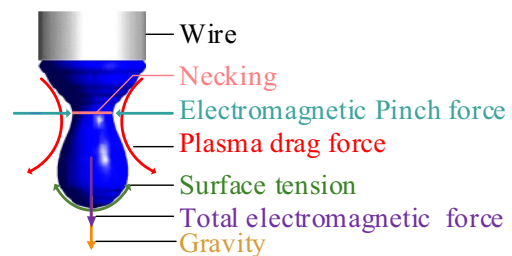


Fig. 15 Schematic diagram of forces acting on a droplet

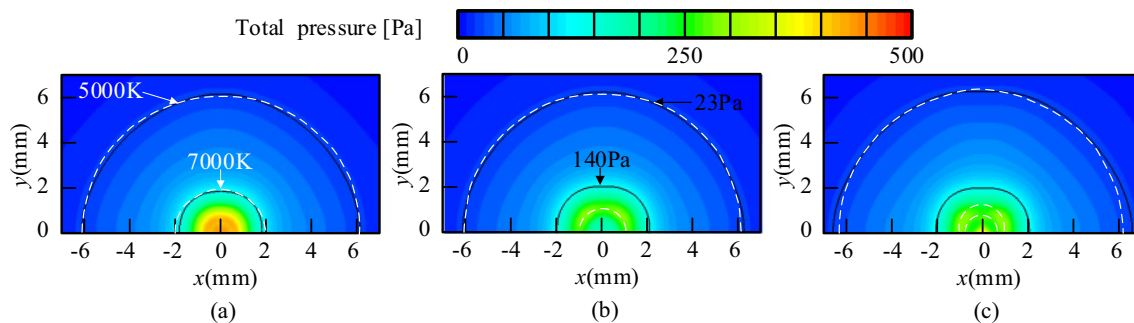
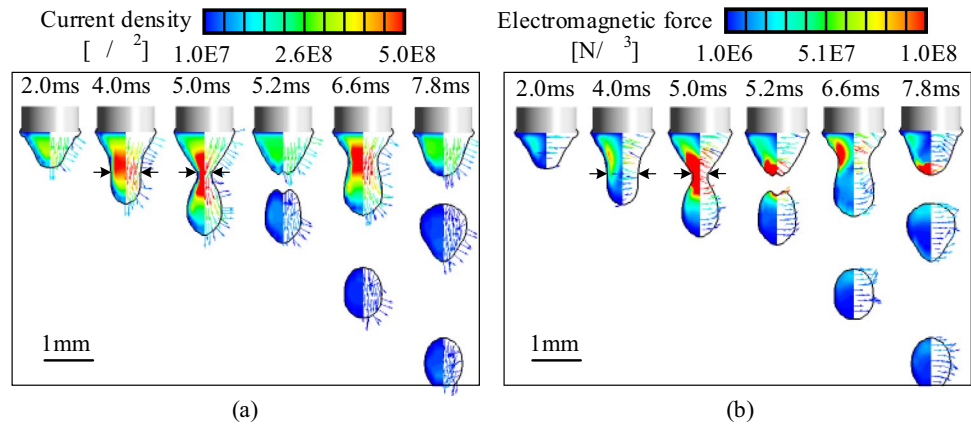


Fig. 14 Arc pressure distribution on workpiece surface: (a) $t = 5.0$ ms, (b) $t = 6.6$ ms and (c) $t = 7.8$ ms

Fig. 16 (a) Current density and (b) electromagnetic force inside the droplet



The effect of the surface tension at the forming droplet was vertical upward to maintain the droplet at the wire tip. It could be calculated by Eq. 24. Before necking, r was the radius of wire. After necking, r was the radius of necking. After separating, r was zero. The resultant of surface tension could be calculated by Eq. 24.

$$F_s = 2\pi r\sigma \tag{24}$$

Before necking, F_s was 4.5×10^{-3} N, and it acted on the liquid–solid interface. After necking, r continued to decrease. At 4.0 ms, r was 0.30 mm, F_s was 2.3×10^{-3} N, and it acted on the outer ring of necking. At 5.0 ms, r was only 0.15 mm, and F_s decreased to 1.1×10^{-3} N, which might not be strong enough to maintain the forming droplet at the wire tip. After separating, F_s was zero.

(3) Electromagnetic force

The electrical conductivity of the molten metal was hundreds of times that of plasma, so the current density inside the forming droplet was much larger than that of the arc, as shown in Fig. 16(a). The current in the droplet could generate an axisymmetric electromagnetic force, as shown in Fig. 16(b).

At 2.0 ms, the forming droplet was hemispherical, and the direction of the current inside the droplet was vertically downward along the wire axis due to its continuity. Its density reached 2.6×10^8 A/m². The total electromagnetic force generated by parallel downward current could be ignored. The electromagnetic pinch force reached 3.0×10^7 N/m³ and contracted inward, which promoted necking. At 4.0 ms, the necking formed, and its section area was one quarter of that of wire. The vertical downward current density increased to 5.0×10^8 A/m². The electromagnetic pinch force of 8.0×10^7 N/m³ was generated at the necking to accelerate its contraction.

At 5.0 ms, the section area of necking was only one sixteenth of that of wire. The current density inside the forming droplet increased first and then decreased from

wire tip to droplet bottom, and it was up to 1.2×10^9 A/m² at the necking. The electromagnetic pinch force of 3.5×10^8 N/m³ was generated at the necking to accelerate its contraction. Below the necking, the electromagnetic pinch force changed from inward to outward, because the radial current at the side of the droplet increased, changing the direction of the induced magnetic field. This kept the forming droplet nearly spherical. Above the necking, the inward sloping current line produced an upward electromagnetic force along the axial direction. Its strength reached 1.6×10^8 N/m³ and the integral reached 1.0×10^{-2} N. Although the duration of the upward force was less than 1ms, it was enough to change the flow direction of molten metal above necking, which hindered the flow of molten metal to the necking.

At 5.2 ms, the first droplet was separated from the wire, and the current density and electromagnetic force inside it decreased rapidly. At 6.6 ms and 7.8 ms, the current density inside the first droplet was basically consistent with its surrounding plasma, reduced to 1×10^7 A/m². The electromagnetic pinch force decreased to 1.1×10^7 N/m³ and pointed outward, which confirmed the formation of low current density channel in the arc inner layer.

The electromagnetic pinch force could form a high pressure to overcome the surface tension, thus promoting necking. Only in the case of severe necking, an upward electromagnetic force was generated above the necking, which intensified necking and promoted droplet transfer.

(4) Plasma drag force

The velocity of the plasma was much higher than that of the droplet, so it generated a downward viscous drag, that was, plasma drag force. It could be calculated by Eq. 25 [38]. Before necking, D_d was the diameter of the sphere equivalent to the volume of molten metal. After necking, D_d was the diameter of the largest cross section below the necking. After separating, D_d was the diameter of droplet.

$$F_{pla} = C_{ds} \frac{1}{2} \rho_g v_g^2 \left(\frac{\pi D_d^2}{4} \right) \quad (25)$$

Before necking, F_{pla} increased continuously. At 2.0 ms, D_d was 0.76 mm, and F_{pla} was 5.6×10^{-4} N. At 4.0 ms, the drag force of the molten metal at wire tip reached 9.0×10^{-4} N, while that below the necking (F_{pla}) was 3.3×10^{-4} N. After necking, F_g continued to increase again, and reached 4.7×10^{-4} N at 5.2 ms.

The above analysis showed that the upward surface tension was the main force to keep the molten metal at the wire tip. The electromagnetic pinch force reduced the necking radius of the droplet, causing a decrease in surface tension, which was the main factor promoting droplet transfer. Gravity and plasma drag force provided acceleration for droplet movement.

3.4.2 Droplet velocity and temperature

Figure 17(a) shows the velocity of droplet at different times. At 0.0 ms, molten metal flowed from the wire tip at a velocity of 0.12 m/s. Then, driven by the plasma drag force, the downward acceleration of molten metal reached 15 times the gravitational acceleration. At 2.0 ms, the maximum downward velocity of molten metal at the wire tip reached 0.66 m/s, and its internal average velocity was 0.3 m/s. At 4.0 ms, the downward velocity at the necking exceeded 1.2 m/s, and its internal average speed increased by 43% compared with 2.0ms. After necking, the total electromagnetic force drove the molten metal above the necking to form an upward reflux. The electromagnetic pinch force produced a high-pressure zone at the necking, driving the molten metal to flow downward. The maximum velocity of the molten metal below the necking exceeded 3.5 m/s at 5.0 ms. The average internal velocity of the droplet increases to 0.67 m/s.

After separating, the velocity of the molten metal inside the droplet became uniform, and it accelerated continuously under the driving of the plasma drag force, impinging the workpiece at a velocity of over 1.3 m/s at 7.8 ms. The high-velocity droplet impingement could generate a strong force [39], which might induce various weld defects, such as finger penetration, undercut, and humping.

The temperature of the droplet was shown in Fig. 17(b). At 0.0 ms, molten metal flowed from the wire tip at a temperature of 1800 K. Under the action of the surrounding high temperature plasma and inside Joule heat, the temperature of molten metal rose rapidly. At 2.0 ms, the surface temperature of the forming droplet reached the boiling point, and a large amount of iron vapor diffused into the plasma. The internal temperature was not uniform. At 5.0 ms, the temperature of molten metal below the necking became relatively uniform, and the average temperature was about 2700 K. After separating, the temperature of the droplet continuously increased, reaching 2800 K at 7.8 ms. The temperature of the droplet was far higher than the average temperature of the molten metal in the weld pool, which might not only cause strong heat convection, increasing the penetration, but also lead to the burning of alloy elements, reducing the weld performance.

In the whole droplet transfer process, the plasma drag force had obvious downward acceleration effect on droplet. The electromagnetic force mainly acted on the necking stage, causing the reverse molten metal flow to promote the separation of the droplet and wire. Droplet temperature was the result of convective heat transfer and Joule heat generation. Before separating, the Joule heat generation inside the droplet was the main source of increasing the droplet temperature. After separating, convective heat transfer from high-temperature plasma played a major role.

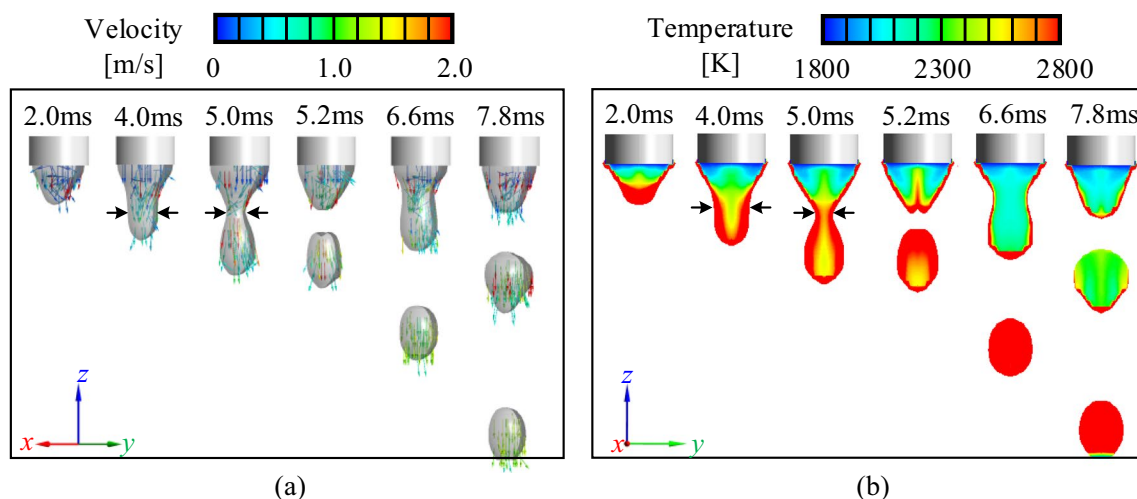


Fig. 17 (a) Velocity and (b) temperature distribution inside the droplet

3.5 Evolution of arc and droplet behaviors

The arc and droplet behaviors changed periodically during welding process. Figure 18 shows the variation of characteristic parameters at different position with time. The point 1 was close to the forming droplet surface, point 2 was in the arc inner layer, point 3 was located at the boundary between the inner layer and arc periphery, and point 4 was in the arc periphery, and point 5 was at the arc edge. The horizontal distances between these points and the welding wire axis were 0.5, 1.0, 2.0, 3.0, and 4.0 mm, respectively. The vertical distances between these points and the wire tip were all 2.0 mm.

Figure 19 (a) illustrates the variations of iron vapor content with time. Before 5.0 ms, the Y_m in the arc rapidly increased as iron vapor spilled out of the forming droplet surface. The closer to the droplet, the higher the Y_m . After 5.0 ms, the arc was in a quasi-steady state. At point 1, Y_m showed significant fluctuations with droplet transfer. At 5.0 ms, the first droplet was necking, and the Y_m was 19.6%. At 5.4 ms, according to the mass spring theory, the radial radius of the droplet just falling off was greater than the axial radius, and the distance from the drop surface to point 1 was reduced, and the Y_m exceeded 25%. After the droplet passed through, Y_m rapidly decreased to 22%. At 7.6 ms, the second droplet passed through point 1, and the Y_m increased to 26%, then rapidly decreased to 23%. The same was true for the third droplet, the Y_m at point 1 exhibited significant periodicity with droplet transfer, which would affect the distribution of current density and temperature. The Y_m of point 2 also showed periodicity with droplet transfer, but the fluctuation was significantly weaker than that of point 1. Y_m of points 3, 4, and 5 stabilized at 11.4%, 8.0% and 6.0%, respectively. The periodicity was not obvious, because these points were far away from the droplet and weakly affected by the droplet transfer.

The variation of current density with time at different positions in the arc was shown in Fig. 19 (b). The current density at point 1 varied considerably at different moments of the droplet transfer. With the first droplet necking at 5.0 ms and the arc temperature reaching 15,000 K, at point 1 the change in the Y_m had little effect on the conductivity and the current density could reach 3.4×10^7 A/m². As the first droplet broke away from the wire tip, a stable iron-rich channel was formed in the arc inner layer. At 7.2 ms and 9.6 ms the new droplet were necked and the current density at point 1 decreased slightly from the current density at point 1 when the first droplet was necked, due to the higher Y_m . At 5.4 ms, 7.6 ms, and 10.2 ms, point 1 near the droplet surface, the heat conduction and absorption of the droplet led to a decrease in temperature, resulting in a decrease in current density to 1.1×10^7 A/m², 3.8×10^6 A/m² and 3.0×10^6 A/m², respectively. It indicated that temperature was the main

factor affecting conductivity. The trend of the current density at point 2 was basically consistent with point 1, but the fluctuation amplitude decreased. As the distance between the point 2 and the arc axis increased, the impact of droplet transfer on its current density decreased. At 5.0 ms, the current density could reach 1.3×10^7 A/m². As the droplet fallen, the conductivity of the surrounding plasma decreased. At 5.4 ms the current density decreased to 1.0×10^7 A/m². After 5.4 ms, the distance between the droplet and point 2 increased, and the current density increased. The current density increased again to 1.5×10^7 A/m² at 6.8 ms. The second droplet grew up subsequently, and the current density was affected by the droplet transfer. At 7.6 ms, the current density decreased again to 9.8×10^6 A/m². Then the current density changed periodically with the new droplet transfer again. The distance from points 3, 4 and 5 to the arc axis were larger. There was no significant fluctuation in the temperature and Y_m , so the conductivity remained stable. The current density was maintained at 5.0×10^6 A/m², 2.6×10^6 A/m² and 1.2×10^6 A/m², respectively.

The temperature changes at different positions in the arc over time were shown in Fig. 19 (c). The temperature at each point in the arc would rapidly decrease before 4.0 ms. The droplet transfer had a dramatic effect on the temperature at point 1. At point 1, the current density was high at 5.0 ms, 7.2 ms and 9.6 ms, and joule heat generation increased, thus the arc temperature would rise; during the process of the droplet detaching from the wire tip and gradually approaching the point 1, the arc temperature would gradually decrease due to the decrease in current density and the influence of the droplet absorbing heat; at 5.4 ms, 7.6 ms, and 10.2 ms, the arc temperature would decrease to 11000K, 8100K, and 8300K, respectively; the rich iron channel formed by the droplet transfer would reach a steadily iron vapor content of more than 20% after 5.4 ms, and the radiation heat dissipation increased, the current density decreased, and the joule heat generation decreased, so the arc temperature at point 1 at 7.6 ms and 10.2 ms was much lower than that at 5.4 ms. As the process of the detaching droplet moving away from point 1, the arc temperature would increase again until the new droplet necked, and the arc temperature culminated at point 1. The droplet didn't absorb much heat at point 2, so the change in current density caused by droplet transfer was the main factor affected the temperature change at point 2, at 5.0 ms, 7.2 ms, and 9.4 ms the current density increased, the arc temperature could reach 11000K; the corresponding decrease in current density at 5.4 ms, 7.6 ms, and 10.2 ms would cause a decrease in arc temperature. After the arc reaches quasi steady state at 5.0 ms, the arc temperature at points 3,4,5 stabilized at 7000 K, 6300 K, and 5300 K, respectively.

The behaviors of the inner arc layer varied periodically with the droplet transfer, while the arc periphery remained stable. When the droplet passed through the inner arc layer,

Fig. 18 (a) Changes in Y_m , (b) changes in current density, (c) changes in temperature

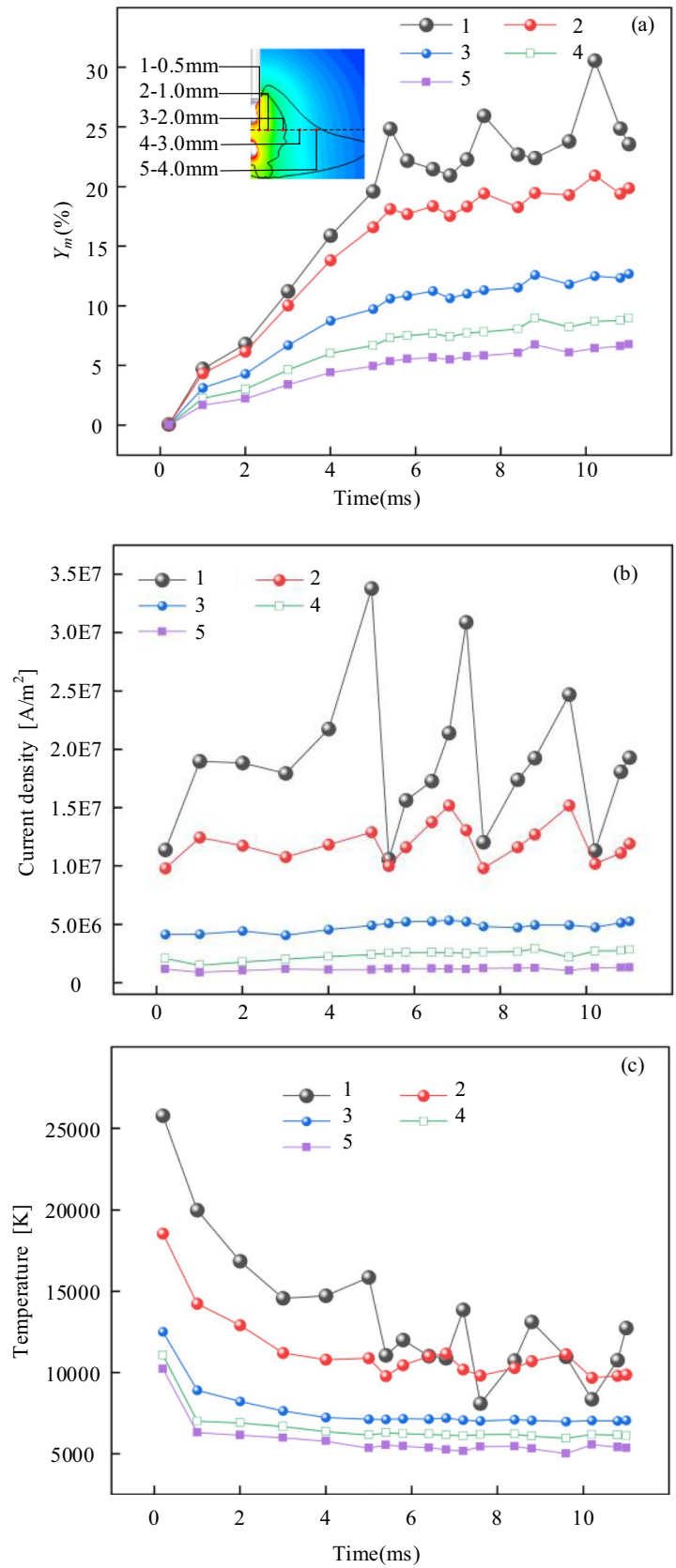
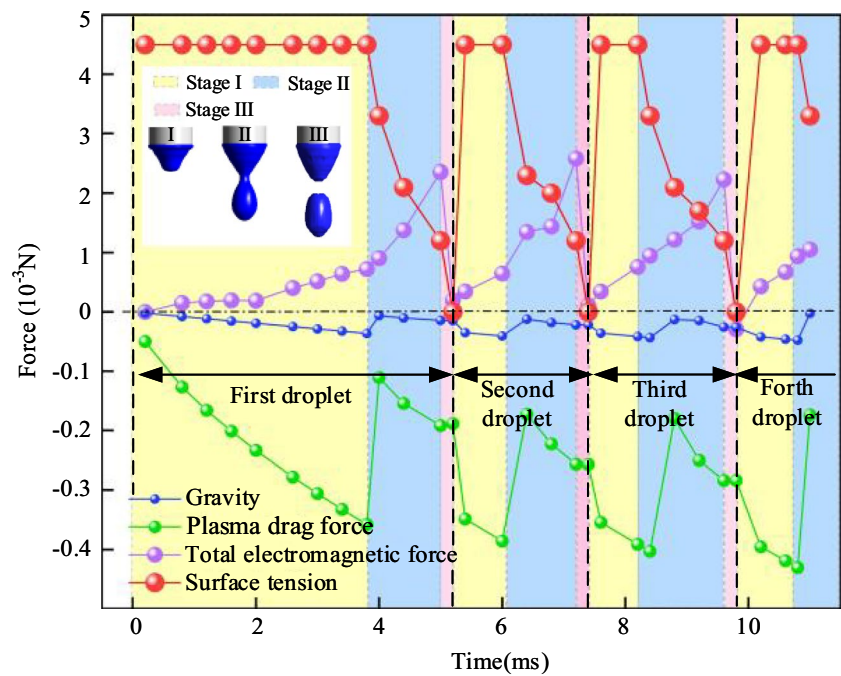


Fig. 19 Changes of axial electromagnetic force, gravity and plasma drag force with time



the decalcescence of the droplet made the inner arc temperature decreased, which reduced the plasma conductivity. The current density reduced, and the heat production in the inner arc layer decreased. Meanwhile, with the increased of Y_m , the heat radiation of plasma increased and the inner arc temperature sharply decreased. After the droplet passed through, the current density increased rapidly, while the radiation heat dissipation decreased, and the temperature in the inner arc layer raised rapidly.

The droplets fallen into the weld pool under the combined effects of gravity, surface tension, electromagnetic force, and plasma drag force. Figure 19 shows the direction and magnitude of gravity, surface tension, total electromagnetic force, and plasma drag force changes with time. The force on droplet varied periodically with time. The first, second, and third droplet detached from the wire tip at 5.2 ms, 7.4 ms, and 9.6 ms, respectively. Each droplet transfer period could be divided into three stages, namely before droplet necking (stage I), necking to separating (stage II), and after separating (stage III).

During the stage I of the first droplet (0–4.0 ms), the surface tension and the total electromagnetic force were upward, and hindered the droplet from detaching from the wire tip. The gravity and plasma drag force were downward. The surface tension maintained 4.5×10^{-3} N. As the current of droplet increased, the total electromagnetic force gradually increased from 0 to 9.0×10^{-4} N. As the droplet grew, the force of gravity increased from 0 to 6.2×10^{-6} N, and the plasma drag force on the droplet also increased from 0 N to 1.0×10^{-4} N. The stage I of the second and third droplet were 5.2–6.0 ms and 7.4–8.2 ms, respectively. At this stage, the

upward force was much greater than the downward force, it was difficult for the droplet to detach from the wire tip, and the droplet at the wire tip gradually grew and elongated under the action of gravity and plasma drag force.

During the stage II of the first droplet (4.0–5.0 ms), the magnitude of the various forces acting on the droplet changed. The elongated droplet underwent necking under the action of electromagnetic pinch force, resulting in a decrease in surface tension at a rate of 4.8×10^{-4} N/s. The droplet below the necking position was more likely to detach from the wire tip. At 4.0 ms, gravity and plasma drag force of droplet below the necking position were 0.7×10^{-5} N and 1.1×10^{-4} N, which gradually increased as the droplet grew. At 5.0 ms, the gravity and plasma drag force of droplet below the necking position reached 2.0×10^{-4} N and 1.4×10^{-5} N. The axial electromagnetic force on the droplet rapidly increased, which was proportional to the square of time. It indicated that the generation of necking was the main factor causing a significant increase in electromagnetic pinch force. The large upward total electromagnetic force caused reflux inside the droplet and reduced the downward flow velocity of the droplet. The stage II of the second and third droplet were 6.0–7.2 ms and 8.2–9.4 ms, respectively. At this stage, the droplet produced necking under the action of electromagnetic pinch force, and the resistant force (surface tension) to droplet transfer gradually decreased.

The stage III was 5.0–5.2 ms. The droplet separated from the wire tip at this stage. The surface tension became zero, and the total electromagnetic force inside the droplet decreased. The droplet was subjected to downward gravity and plasma drag force, with a value of -2.1×10^{-4} N,

providing downward acceleration for the droplet. The stage III of the second and third droplet were 7.2–7.4 ms and 9.4–9.6 ms, respectively.

After the first droplet separated, there was still molten metal at the wire tip, and during the transfer of the second droplet and third droplet, the time for the droplet to elongate and grow up was shortened in the stage I. At stage II, the second and third droplet were similarly with the first droplet, necking occurred and the resistance to drop transfer was reduced. At stage III, the separating droplet under the combined force of the downward axial force, the droplet fallen into the weld pool. The force state of the droplet exhibited a clear periodic trend over time.

Figure 20 shows the variation of upward resultant force and downward resultant force over time. The upward axial resultant force was composed of total electromagnetic force and surface tension, which hindered the droplet transfer. The downward axial resultant force was composed of gravity and plasma drag force. In stage I, the increase in axial electromagnetic force caused the upward resultant force rising. The upward resultant force from 4.5×10^{-3} N increased to 5.2×10^{-3} N. The downward resultant force from -5.2×10^{-5} N increased to -4.0×10^{-4} N. In stage II, the surface tension decreased, the total electromagnetic force increased, and the upward resultant force decreased to 3.5×10^{-3} N. The value of the upward resultant force had a greater relationship with the surface tension. In stage III, necking fractured, surface tension decreased to zero, and total electromagnetic force decreased, the upward force sharply decreased to 1.0×10^{-4} N. The plasma drag force was much greater than gravity, which was the main factor

caused the downward force to change. The downward force on the before necking droplet reached -4.0×10^{-4} N, the downward force was only -2.1×10^{-4} N. It indicated that the main reason for the detachment of the droplet was the decrease in surface tension caused by electromagnetic pinch force.

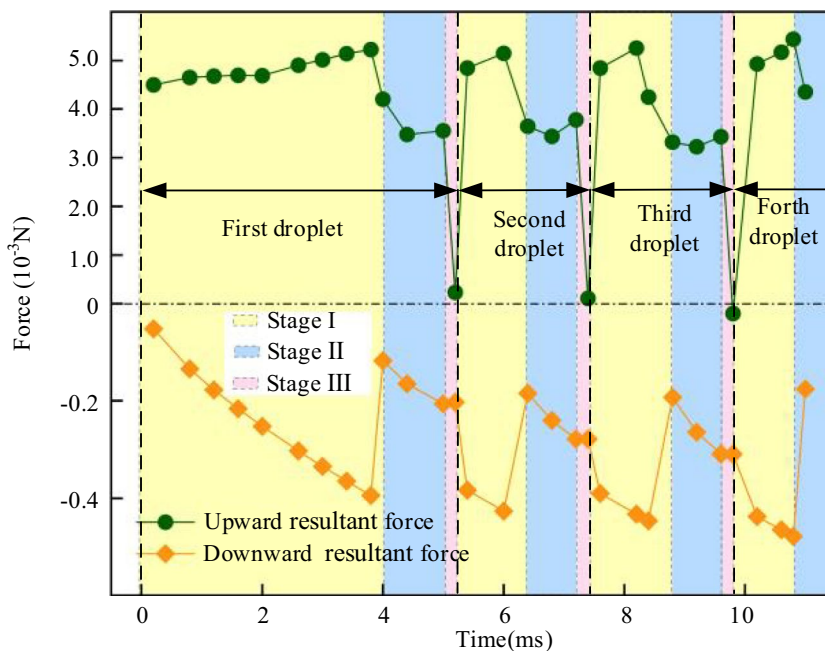
The electromagnetic force and surface tension were the main factors affecting the separation of droplet and wire tip. The electromagnetic pinch force promoted the necking of the droplet and decreased the upward surface tension. After the droplet detached from the wire tip, the downward acceleration of the droplet was mainly provided by the plasma drag force. The droplet into the weld pool under the combined axial force with the speed of 1.3m/s. The behavior of arc and droplet transfer exhibited significant periodicity over time.

4 Conclusions

The arc and droplet behaviors in GMAW were investigated using a 3D multi-physics coupling transient model. The simulation results were in good agreement with the experimental results. The following conclusions were obtained:

(1) The iron vapor from the surface of the droplet generated an iron rich channel in the arc inner layer, which changed the physical parameters of the plasma and reduced the arc temperature. The droplet transfer increased the electromagnetic force at the lower half of the arc inner layer, causing the arc inner layer to contract upwards.

Fig. 20 Change of surface tension and downward axial force with time



(2) The distribution of current density, temperature and pressure on the workpiece surface were basically consistent with Gaussian distribution. The droplet transfer could cause shrinkage in the high-temperature area, but it had little effect on the pressure distribution, which provided a theoretical guidance for more in-depth and accurate analysis of the influence of arc-droplet on the heat and mass transfer behavior of weld pool.

(3) The surface tension decreased to zero under the action of electromagnetic pinch force, which was the main factor causing droplet transfer. The plasma drag force and gravity provided downward acceleration for the droplet. The separating droplet was heated by arc heat, and its temperature could reach 2800 K. The high temperature droplet impinged on the workpiece at a speed of 1.3 m/s.

(4) The arc and droplet transfer behaviors exhibited significant periodicity over time. Changes in the Y_m of arc inner layer could affect the arc behavior. The magnitude of the upward axial resultant force exerted on the droplet was mainly related to the value of surface tension. The downward acceleration of the droplet was mainly provided by the plasma drag force.

Acknowledgements This work was supported by the National Natural Science Foundation of China [grant numbers 51905321], Shandong Provincial Natural Science Foundation [grant number ZR2021ME136], and Shandong Provincial Key Laboratory of Precision Manufacturing and Non-traditional Machining.

Data availability The authors will supply the relevant data in response to reasonable requests.

Declarations

Conflict of interests The authors declare no competing interests.

Disclaimer We also declare that we do not have any commercial or associative interest that represents a conflict of interest in connection with the work entitled “Multi-physics coupling simulation of GMAW arc and droplet behaviors based on CFD”.

References

- Hu J, Tsai H, Wang P (2007) Numerical Modeling of GMAW ARC. *Advances in Computer, Information, and Systems Sciences, and Engineering*. Springer, Dordrecht, pp. 69–74. https://doi.org/10.1007/1-4020-5261-8_12
- Madavi KR, Jogi BF, Lohar GS (2022) Metal inert gas (MIG) welding process: A study of effect of welding parameters. *Mater Today: Proc* 51(1):690–698. <https://doi.org/10.1016/j.matpr.2021.06.206>
- Suban M, Tušek J (2001) Dependence of melting rate in MIG/MAG welding on the type of shielding gas used. *J Mater Process Technol* 119(1–3):185–192. [https://doi.org/10.1016/S0924-0136\(01\)00940-2](https://doi.org/10.1016/S0924-0136(01)00940-2)
- Gleizes A (2015) Perspectives on Thermal Plasma Modelling. *Plasma Chem Plasma Process* 35:455–469. <https://doi.org/10.1007/s11090-014-9589-2>
- Murphy AB (2011) A self-consistent three-dimensional model of the arc, electrode and weld pool in gas–metal arc welding. *J Phys D: Appl Phys* 44(19):194009. <https://doi.org/10.1088/0022-3727/44/19/194009>
- Zhao Y, Chung H (2017) Numerical simulation of droplet transfer behavior in variable polarity gas metal arc welding. *Int J Heat Mass Transfer* 111:1129–1141. <https://doi.org/10.1016/j.ijheatmasstransfer.2017.04.090>
- Wang L, Chen J, Wu CS, Luan SC (2020) Numerical analysis of arc and droplet behaviors in gas metal arc welding with external compound magnetic field. *J Mater Process Technol* 282:116638. <https://doi.org/10.1016/j.jmatprotec.2020.116638>
- Nemchinsky VA (1994) Size and shape of the liquid droplet at the molten tip of an arc electrode. *J Phys D: Appl Phys* 27(7):1433–1442. <https://doi.org/10.1088/0022-3727/27/7/014>
- Kim Y, Eagar T (1993) Metal transfer in pulsed current gas metal arc welding. *Weld J* 72(7): 279–87. <https://api.semanticscholar.org/CorpusID:165159041>
- Joo TM, Yoo CD, Lee TS (1996) Effects of welding conditions on molten drop geometry in arc welding. *J Manuf Sci Eng* 118(4):623–7. <https://doi.org/10.1115/1.2831076>
- Hirt CW, Nichols BD (1981) Volume of fluid (VOF) method for the dynamics of free boundaries. *J Comput Phys* 39(1):201–225. [https://doi.org/10.1016/0021-9991\(81\)90145-5](https://doi.org/10.1016/0021-9991(81)90145-5)
- Chol S K, Ko S H, Yoo C D, Kim Y S (1998) Dynamic simulation of metal transfer in GMAW-part 2: short-circuit transfer mode. *Weld J* 77: 45–51. <https://api.semanticscholar.org/CorpusID:138551542>
- Fan HG, Kovacevic R (1999) Droplet formation, detachment, and impingement on the molten pool in gas metal arc welding. *Metall Mater Trans B* 30(4):791–801. <https://doi.org/10.1007/s11663-999-0041-6>
- Tashiro S, Tanaka M, Nakata K, Iwao T, Koshiishi F, Suzuki K, Yamazaki K (2007) Plasma properties of helium gas tungsten arc with metal vapour. *Sci Technol Weld Joining* 12(3):202–207. <https://doi.org/10.1179/174329307X164391>
- Schnick M, Fuessel U, Hertel M, Haessler M, Spille-Kohoffand A, Murphy AB (2010) Modelling of gas–metal arc welding taking into account metal vapour. *J Phys D: Appl Phys* 43(43):434008. <https://doi.org/10.1088/00223727/43/43/434008>
- Ogino Y, Hirata Y, Asai S (2020) Discussion of the Effect of Shielding Gas and Conductivity of Vapor Core on Metal Transfer Phenomena in Gas Metal Arc Welding by Numerical Simulation. *Plasma Chem Plasma Process* 40:1109–1126. <https://doi.org/10.1007/s11090-020-10102-1>
- Nomura K, Yoshii K, Toda K, Mimura K, Hirata Y, Asai S (2017) 3D measurement of temperature and metal vapor concentration in MIG arc plasma using a multidirectional spectroscopic method. *J Phys D: Appl Phys* 50(42):425205. <https://doi.org/10.1088/1361-6463/aa8793>
- Wang LL, Wang HP, Lu FG, Murphy AB, Carlson BE (2014) Numerical analysis of Al vapour effects in gas metal arc welding of Al alloys. *Sci Technol Weld Joining* 19(5):361–368. <https://doi.org/10.1179/1362171814Y.0000000200>
- Murphy AB (2010) The effects of metal vapour in arc welding. *J Phys D: Appl Phys* 43(43):434001. <https://doi.org/10.1088/0022-3727/43/43/434001>
- Schnick M, Fuessel U, Hertel M, Spille-Kohoff A, Murphy AB (2009) Metal vapour causes a central minimum in arc temperature in gas–metal arc welding through increased radiative emission. *J Phys D: Appl Phys* 43(2):022001. <https://doi.org/10.1088/0022-3727/43/2/022001>

21. Schnick M, Hertel M, Fuessel U, Uhrlandt D (2013) Energy balance in MIG arcs. *J Phys D: Appl Phys* 46(22):224002. <https://doi.org/10.1088/0022-3727/46/22/224002>
22. Haidar J (2010) The dynamic effects of metal vapour in gas metal arc welding. *J Phys D: Appl Phys* 43(16):165204. <https://doi.org/10.1088/0022-3727/43/16/165204>
23. Hertel M, Rose S, Füssel U (2016) Numerical simulation of arc and droplet transfer in pulsed GMAW of mild steel in argon. *Weld World* 60:1055–1061. <https://doi.org/10.1007/s40194-016-0362-4>
24. Ogino Y, Hirata Y (2015) Numerical simulation of metal transfer in argon gas-shielded GMAW. *Weld World* 59:465–473. <https://doi.org/10.1007/s40194-015-0221-8>
25. Han Y, Chen J, Ma H, Zhao X, Wu C, Gao J (2020) Numerical simulation of arc and droplet behaviors in TIG-MIG hybrid welding. *Materials* 10(20):4253. <https://doi.org/10.3390/ma13204520>
26. Hu J, Tsai H L (2007) Heat and mass transfer in gas metal arc welding. Part I: The arc. *Int J Heat Mass Transfer* 50(5–6):833–846. <https://doi.org/10.1016/j.ijheatmasstransfer.2006.08.025>
27. Brackbill JU, Kothe DB, Zemach C (1992) A continuum method for modeling surface tension. *J Comput Phys* 100(2):335–354. [https://doi.org/10.1016/0021-9991\(92\)90240-Y](https://doi.org/10.1016/0021-9991(92)90240-Y)
28. Shin S, Lee WI (2000) Finite element analysis of incompressible viscous flow with moving free surface by selective volume of fluid method. *Int J Heat Fluid Flow* 21(2):197–206. [https://doi.org/10.1016/S0142-727X\(99\)00083-1](https://doi.org/10.1016/S0142-727X(99)00083-1)
29. Wilke CR (1950) A Viscosity Equation for Gas Mixtures. *J Chem Phys* 18(4):517–519. <https://doi.org/10.1063/1.1747673>
30. Tanaka M, Yamamoto K, Tashiro S, Nakata K, Yamamoto E, Yamazaki K, Suzuki K, Murphy AB, Lowke JJ (2010) Time-dependent calculations of molten pool formation and thermal plasma with metal vapour in gas tungsten arc welding. *J Phys D: Appl Phys* 43(43):434009. <https://doi.org/10.1088/0022-3727/43/43/434009>
31. Hirata Y (1994) Physics of welding—melting rate and temperature distribution of electrode wire. *Weld Int* 9(5):348–351. <https://doi.org/10.1080/09507119509548811>
32. Modenesi PJ, Reis RI (2007) A model for melting rate phenomena in GMA welding. *J Mater Process Technol* 189(1):199–205. <https://doi.org/10.1016/j.jmatprotec.2007.01.022>
33. Xu B, Chen S, Jiang F, Phan HL, Tashiro S, Tanaka M (2018) The influence mechanism of variable polarity plasma arc pressure on flat keyhole welding stability. *J Manuf Process* 37:519–528. <https://doi.org/10.1016/j.jmapro.2018.12.026>
34. Zong R, Chen J, Wu C. S., G. K. Padhy, (2017) Influence of molten metal flow on undercutting formation in GMAW. *Sci Technol Weld Joining* 22(3) 198–207. <https://doi.org/10.1080/13621718.2016.1214406>
35. Ran Z, Chen J, Wu CS (2020) A comparison of double shielded GMAW-P with conventional GMAW-P in the arc, droplet and bead formation. *J Mater Process Technol* 1 285:116781. <https://doi.org/10.1016/j.jmatprotec.2020.116781>
36. Hirata Y (2003) Pulsed arc welding *Weld Int* 17:98115. <https://doi.org/10.1533/wint.2003.3075>
37. Zong R, Chen J, Wu CS (2019) A comparison of TIG-MIG hybrid welding with conventional MIG welding in the behaviors of arc, droplet and weld pool. *J Mater Process Technol* 270:345–355. <https://doi.org/10.1016/j.jmatprotec.2019.03.003>
38. Xu G, Hu J, Tsai HL (2009) Three-dimensional modeling of arc plasma and metal transfer in gas metal arc welding. *Int J Heat Mass Transfer* 52(7):1709–1724. <https://doi.org/10.1016/j.ijheatmasstransfer.2008.09.018>
39. Murphy AB, Thomas DG (2017) Prediction of arc, weld pool and weld properties with a desktop computer model of metal–inert-gas welding. *Weld World* 61:623–633. <https://doi.org/10.1007/s40194-017-0444-y>

Publisher's Note Springer Nature remains neutral with regard to jurisdictional claims in published maps and institutional affiliations.

Springer Nature or its licensor (e.g. a society or other partner) holds exclusive rights to this article under a publishing agreement with the author(s) or other rightsholder(s); author self-archiving of the accepted manuscript version of this article is solely governed by the terms of such publishing agreement and applicable law.